nature portfolio

https://doi.org/10.1038/s41586-021-03248-1

Supplementary information

Propagation of large earthquakes as self-healing pulses or mild cracks

In the format provided by the authors and unedited

Supplementary Information

Materials and Methods

Supplementary Text

Figs. S1 to S23

Tables S1 to S6

Captions for Videos S1 to 3

Materials and Methods

Model description

To conduct numerical simulations of long-term fault behavior including earthquake sequences and aseismic slip, we utilize the spectral boundary integral method to solve the elastodynamic equations of motion coupled with friction boundary conditions, including the evolution of pore fluid pressure and temperature on the fault coupled with off-fault diffusion[32,49]. Our simulations consider mode III slip on a 1-D fault embedded into a 2-D uniform, isotropic, elastic medium. At each time step, slip rates and shear tractions are calculated for each cell of the discretized fault by equating fault shear stress to frictional shear resistance. The evolution of shear stress at each cell depends on loading conditions as well as coupled interactions with slip at other fault cells through wave-mediated static and dynamic stress transfers. The use of adaptive time-stepping in our methodology allows us to resolve earthquake sequences in their entirety, including the sponta-

neous nucleation process, dynamic rupture propagation, postseismic slip following rupture events, and the interseismic period between events that can last up to tens or hundreds of years.

In all of our fault models, we use the laboratory-derived Dieterich-Ruina rate-and-state friction law with the state evolution governed by the aging law[50,51,53]:

$$\tau = \overline{\sigma} f(V, \theta) = (\sigma - p) \left[f_* + a \log \frac{V}{V_*} + b \log \frac{\theta V_*}{L} \right], \tag{S1}$$

$$\dot{\theta} = 1 - \frac{V\theta}{L}, \tag{S2}$$

where $\overline{\sigma}$ is the effective normal stress, σ is the normal stress, p is the pore fluid pressure, f_* is the reference steady-state friction coefficient at reference sliding rate V_*, L is the characteristic slip distance, and a and b are the direct effect and evolution effect parameters, respectively. Other formulations for the evolution of the state variable exist, such as the slip law[51] as well as various composite laws, and the formulation that best describes various laboratory experiments remains a topic of ongoing research[54]. However, the choice of the state evolution law should not substantially influence the results of this study, as the evolution of shear resistance during dynamic rupture within our simulations is dominated by the presence of enhanced weakening mechanisms. We use the version of the expressions (S1-S2) regularized for zero and negative slip rates[32].

During conditions of steady-state sliding ($\dot{\theta} = 0$), the friction coefficient is expressed as:

$$f_{ss}(V) = f_* + (a - b) \log \frac{V}{V_*}. \tag{S3}$$

The combination of frictional properties $(a - b) > 0$ results in steady-state velocity-strengthening (VS) behavior, where stable slip is expected, and properties resulting in $(a - b) < 0$ lead to steady-

state velocity-weakening (VW) behavior, where accelerating slip and hence stick-slip occur for sufficiently large regions. The total fault domain of size λ is partitioned into a frictional region of size λ_{fr} where we solve for the balance of shear stress and frictional shear resistance, as well as a loading region at the edges where the fault is prescribed to slip at a tectonic plate rate (Supplementary Fig. S14). The frictional interface is composed of a region with velocity-weakening frictional properties of size λ_{VW}, surrounded by a velocity-strengthening domain. Most simulations are performed on a fault with a 24-km VW region, however we perform some additional studies with a 50-km VW region to verify that our results are consistent for longer fault models. Values for parameters used in our simulations are provided in Supplementary Tables S1-5.

Note that the concept of "static strength" is not uniquely defined in such rate-and-state formulations of shear resistance in which slip rate is non-zero for any non-zero shear stress of the regularized friction formulation. Even if slip is prescribed at a fixed sliding rate, friction depends on the history of previous slip through the evolution of the state variable, which aims to capture the evolution of local contacts. However, at each fixed sliding rate V, the friction eventually evolves to the steady-state value $f_{ss}(V)$ given by (S3). While that steady-state value depends on the sliding rate, the dependence is relatively minor, as it is logarithmic and $(a-b) \sim 0.01$ or less. We refer to this collection of similar friction values at slow slip rates appropriate for fault creep and earthquake nucleation as "quasi-static" friction coefficient. The product of this quasi-static friction coefficient and the effective confining stress (normal stress minus pore fluid pressure p) gives the shear resistance of faults at slow sliding rates, which we call quasi-static strength. As the representative value of such quasi-static strength, we choose the shear resistance of the fault steadily creeping at

the prescribed long-term tectonic plate rate V_{plate} with the interseismic value of the pore pressure p_{int} (i.e. the value of pore pressure not affected by thermal pressurization of pore fluids):

$$\tau^{\text{strength}}_{\text{quasi-static}} = \tau_{ss}(V_{\text{plate}}) = (\sigma - p_{\text{int}}) \left[f_* + (a-b) \log \left(\frac{V_{\text{plate}}}{V_*} \right) \right]. \tag{S4}$$

Laboratory experiments have shown that the standard rate-and-state laws (Equations S1-S2) work well for relatively slow slip rates (10^{-9} to 10^{-3} m/s). However, at higher slip rates, including average seismic slip rates of $\sim$1 m/s, additional dynamic weakening mechanisms, such as thermal pressurization, can be present. Thermal pressurization occurs when pore fluids within the fault shearing layer heat up, expand, and pressurize during dynamic rupture, reducing the effective normal stress, and therefore shear resistance[6,32,55]. Thermal pressurization is governed in our simulations by the following coupled differential equations for pore pressure and temperature evolution[32]:

$$\frac{\partial p(y,z;t)}{\partial t} = \alpha_{\text{hy}} \frac{\partial^2 p(y,z;t)}{\partial y^2} + \Lambda \frac{\partial T(y,z;t)}{\partial t}, \tag{S5}$$

$$\frac{\partial T(y,z;t)}{\partial t} = \alpha_{\text{th}} \frac{\partial^2 T(y,z;t)}{\partial y^2} + \frac{\tau(z;t) V(z;t)}{\rho c} \frac{\exp(-y^2/2w^2)}{\sqrt{2\pi} w}, \tag{S6}$$

where T is the temperature of the pore fluid, α_{hy} is the hydraulic diffusivity, α_{th} is the thermal diffusivity, τV is the source of shear heating distributed over a Gaussian shear layer of half-width w, ρc is the specific heat, y is the distance normal to the fault plane, and Λ is the coupling coefficient that gives pore pressure change per unit temperature change under undrained conditions.

The efficiency of the thermal pressurization process depends on the interplay of several parameters, where it may be the dominant weakening mechanism during unstable slip for some physical regimes [6,56]. Shear heating, τV, must be strong enough to raise the temperature, given both

the specific heat of the rock, ρc, and the half-width of the shear zone, w. Furthermore, this heat generation must not be dissipated too quickly by the thermal diffusivity, α_{th}, of the system. If sufficient heat is generated, the temperature of the system increases, and this increase is coupled into an increase in pressure of the fluid. The fluid then pressurizes as long as the hydraulic diffusivity, α_{hy}, is not too large. Some of these parameters are relatively well constrained from laboratory experiments: α_{th} = 10^{-6} m/s and ρc = 2.7 MPa K[13,32,57]. The change in pore pressure given a degree increase in temperature is described by the coupling coefficient Λ, which depends on the extent of damage and inelastic dilation around the shearing layer, with typical values ranging from 0.1 for highly damaged wall rock to 1 MPa/K for intact wall rock[6,57]. Two other parameters that substantially control the efficiency of thermal pressurization are the half-width of the shear zone w and hydraulic diffusivity α_{hy}, which can vary significantly: w can vary from 10^{-3} m to 10^{-1} m and α_{hy} can vary from 10^{-2} m^2/s to 10^{-6} m^2/s [6]. Changing these two parameters within these ranges can make thermal pressurization either very efficient or completely negligible. The values we have chosen are motivated by prior studies[6,32] as well as our goal of examining ruptures with both efficient and inefficient enhanced dynamic weakening. In our simulations, we use uniform values for all hydrothermal properties other than w throughout the entire domain, as indicated in Tables S1, S3. w is set to the values shown in Table S3 within the VW region, and then smoothly expands, over a 1 km region at the transition to the VS regions, to a 1-m shearing layer, so that thermal pressurization is effectively disabled in the VS regions.

In addition to thermal pressurization, we also consider a model with enhanced dynamic weakening due to flash heating[6], which has been shown to be efficient at generating self-healing

pulses[22,58]. Flash heating occurs when highly stressed microcontacts heat up dramatically during rapid slip and weaken dynamically. This process is often modeled with a characteristic slip velocity V_w at which flash heating activates. The friction coefficient then evolves to a residual level f_w and remains there during rapid sliding. To model flash heating, we make slight modifications to our steady-state rate-and-state equations to take into account the weakening following[52]:

$$f_{ss}(V) = f(V, \theta_{ss}(V)) = \frac{f(V, L/V) - \frac{V}{|V|} f_w}{1 + |V|/V_w} + \frac{V}{|V|} f_w \tag{S7}$$

where V is the slip rate on the fault, V_w is the characteristic slip velocity at which flash heating becomes effective, and f_w is the residual friction coefficient. Values for parameters used in our simulations with flash heating are provided in Table S4.

Other mechanisms can act in the fault shear zone to produce similar enhanced weakening effects to thermal pressurization, including the thermal decomposition of rocks[59,60], macroscopic melting[15,61,62], elastohydrolubrication [63], and silica gel formation[61–63]. We use thermal pressurization in most of our simulations to demonstrate the effects of enhanced dynamic weakening, however the effects should be qualitatively consistent for other weakening mechanisms.

Earthquakes can nucleate only if the steady-state velocity-weakening region is larger than the nucleation size h^*. For 2D problems, two theoretical estimates of the nucleation size in mode III are [64,65]:

$$h^*_{RR} = \frac{\pi}{4} \frac{\mu L}{(b-a)(\sigma - p)}; h^*_{RA} = \frac{2}{\pi} \frac{\mu L b}{(b-a)^2(\sigma - p)} \tag{S8}$$

where μ is the shear modulus. Another important physical length-scale is the cohesive zone which represents the region at the rupture front under which the primary breakdown in shear resistance

occurs. The quasi-static estimate of the cohesive zone Λ_0 is given as:

$$\Lambda_0 = C_1 \frac{\mu}{W} \tag{S9}$$

with C_1 being a constant and the weakening rate $W = \frac{b\overline{\sigma}}{L}$ for the standard rate-and-state friction law. As the rupture speed increases to the limiting wave speed c_L (c_L is the shear wave speed in mode III), the cohesive zone collapses towards zero. Stronger rate-weakening mechanisms, such as thermal pressurization and flash heating, result in much larger weakening rates and reductions in the cohesive zone size, such that the criterion for sufficient numerical resolution becomes far more restrictive.

Previous studies established that $\Lambda_0/\Delta z$ of 3 to 5 is required to resolve dynamic ruptures with relatively mild weakening imposed through linear slip-weakening friction[66]. However we find that this is not sufficient with more efficient enhanced dynamic weakening, such as that which results in self-healing pulses. If one considers adiabatic and undrained conditions, then an upper bound for the weakening rate due to thermal pressurization can be expressed as[32],

$$W_{TP} = \frac{f\tau\Lambda}{\sqrt{2\pi}w\rho c}. \tag{S10}$$

For the simulations with the most efficient thermal pressurization in this study ($f_{\text{peak}} \approx 0.9$, $\tau_{\text{peak}} \approx 45$ MPa, $\Lambda = 0.34$ MPa/K and $w = 1$ mm), W_{TP} is about 2035 MPa/m, which is five to six times larger than the weakening rate from rate-and-state friction $W_{RS} = 375$ MPa/m. We therefore use a spatial discretization of $\Delta z = 3.3$ m which resolves the quasi-static cohesive zone estimate by at least 25 cells and the nucleation size with more than 88 cells. This more stringent resolution

criterion motivates the choice of 2-D calculations for this study. We have compared the results of our 2-D simulations with fully dynamic 3-D simulations for models with milder enhanced dynamic weakening and find qualitatively similar results.

Methodologies for computing seismological inferences

In our dynamic simulations, the slip and stress evolution is computed at every point along the fault at all times. As such, we are able to calculate the the local and average energy quantities, stress and slip directly in our models (Supplementary Fig. S15). We utilize the averaging methodology of Noda and Lapusta (2012 to compute the energetically averaged properties directly from the local properties along the fault. The initial distribution of shear traction on the fault before an earthquake is denoted by $\tau^{\text{ini}}(z)$. An earthquake produces a slip distribution $\delta(z)$ and the traction along the fault changes to $\tau^{\text{fin}}(z)$. In our models, there is small non-zero slip everywhere on the fault during every event due to the nature of the rate-and-state framework. In terms of determining the area associated with the dynamic rupture process, it is appropriate to only consider points where the inertial term becomes significant. However, there is no exact quantitative criterion to define that. Hence we follow prior studies[47,49,67,68] by defining the ruptured domain Σ to consist of locations that exceed a threshold slip rate of V_{th}:

$$\Sigma = \{\underline{z} \in \Omega | \underline{V}(\underline{z}) > V_{\text{th}}\}. \tag{S11}$$

There is a sharp falloff in slip rate outside the ruptured area down to the creeping rate many orders of magnitude below the seismic slip rate. Thus, changing the threshold by even an order of magnitude or two does not change the rupture size appreciably. For the simulations presented in this study, we use a threshold of $V_{\text{th}} = 0.01$ m/s. We have explored the sensitivity of the rupture

area calculated based on V_{th} ranging from 10^{-3} to 10^{-1} m/s and find minor variations, within 1%. Given this criterion for the rupture area, we are able to calculate all of the averaged and energetic quantities directly from the local properties along the fault.

For natural earthquakes, it is difficult to precisely determine the rupture area due to non-uniqueness and smoothing during inversion procedure. For large events, the rupture shape and dimension may be determined from finite-fault inversions, along with the corresponding local changes in slip and stress, depending on the parameterization of the inversion, including the choice of a minimum slip threshold for a given region to slip before being considered part of the ruptured area[24,68–70]. Note that many seismological studies infer average slip, moment-based stress drops, and rupture dimensions for earthquakes based on spectral representations of the seismic waveforms fitted by a model based on a circular crack with constant rupture speed[6,26,27]. The stress drop consistent with energy partitioning is the energy-based or slip-weighted stress drop, which was proven to always be larger than the moment-based estimate[68]. This reality, along with resolution limitations and the application of smoothing during inversions, suggest that seismologically estimated average stress drops most likely provide lower estimates for the needed energy-based stress drops for energy partitioning[68,71]. Some recent studies used finite-fault inversions to estimate energy-based stress drops directly[24].

In this study, we compare the averaged source properties from our simulated ruptures with published seismological inferences from 114 large ($M_w \geq 7.0$) megathrust earthquakes between 1990 and 2015[24], as well as inferences from the large crustal earthquakes shown in Table S6.

The inferences for megathrust earthquakes, such as the energy-based stress drops, are based on teleseismic finite fault inversions, where the final rupture models depend on the choice of rupture speed in the parameterization of the inversion. For the comparisons in this study, we utilize the results of published finite fault inversions with a rupture speed of 2.5 km/s[24].

Only moment-based estimates of static stress drop can be determined for the large crustal earthquakes, given published inferences of seismic moment and rupture dimensions. The estimates of the moment-based stress drop vary by about a factor of 2 given the assumed geometry of the source region and the dimensions inferred from published finite fault inversions. These estimates of moment-based stress drop most likely represent lower bounds for the energy-based stress drop, which is the more appropriate stress drop for considerations of energy partitioning. Published teleseismic and regional estimates of radiated energy for the large crustal earthquakes in Table S6 vary by about a factor of 4 within the published references.

Shear heating during frictional sliding

We aim to explore conditions compatible with the inferred low-stress, low-heat operation of mature faults. In addition, as the constitutive behavior in our simulations does not account for the production of macroscopic melt, maintaining temperatures below those for which substantial melt formation would be expected is important for producing models that are physically self-consistent. Frictional formulations such as standard rate-and-state laws as well as flash heating do not depend on macroscopic temperature changes and are therefore mathematically agnostic to the localization of shear and corresponding shear heating. We monitor the temperature changes throughout all of

our simulations and use the results from only those simulations in which temperatures remain below 1000 ^{0}C, a representative equilibrium melting temperature for granitic compositions in Earth's crust[6]. Figure S17 illustrates the evolution of maximum fault temperature change over sequences of earthquakes and slow slip for the three models shown in Fig. 3 of the main text.

The rate of shear heating during sliding on a frictional interface is proportional to the shear resistance and sliding rate, τV, and the average shear stress associated with dissipation and heat generation can be calculated as:

$$\tau_{\text{heat}}(t) = \frac{\int_0^t \int_\Omega \tau(z,t')V(z,t')dzdt'}{\int_0^t \int_\Omega V(z,t')dzdt'} \tag{S12}$$

where Ω is the area of the fault interface. The associated temperature increase due to distributed shear within a shearing layer heavily depends upon the degree of localization. Let us consider the temperature rise due to slip distributed over a Gaussian shear layer with half-width, w. The temperature rise at the center of the layer as a function of time can be expressed as[6]:

$$T(0,t) = \frac{1}{\rho c}\int_0^t \frac{\tau(t')V(t')dt'}{\sqrt{2\pi}\sqrt{w^2 + 2\alpha_{th}(t-t')}} \tag{S13}$$

where α_{th} is the thermal diffusivity and ρc is the specific heat. In the simplified case of dissipation due to sliding at a fixed slip rate and a fixed residual stress level, ignoring any dissipation associated with the breakdown process during a rupture, the peak temperature change as a function of the shear zone half-width and the prescribed dynamic resistance level, assuming 1 and 5 meters of slip at $V = 1$ m/s, is shown in Supplementary Fig. S18. Substantial temperature increase is expected as the shearing layer becomes localized between 1 - 10 mm, except for very low dynamic resistance levels. For $w = 1$ mm, temperatures would be expected to increase by over 1000^o C if the dynamic

resistance is greater than 3 MPa. Even for a much broader layer of $w = 10$ mm, substantial temperature increase would be expected for sliding at stress levels above 10 MPa. Note that, for slip rates higher than 1 m/s as commonly observed in dynamic rupture simulations, the shear heating production rate increases, leading to even higher temperatures. In addition, this consideration ignores the dissipation associated with the breakdown process, which may be comparable to or even greater than the dissipation at low residual stress levels.

Approximation for off-fault plasticity

As enhanced dynamic weakening can lead to rapid and large dynamic stress changes, the slip rates in models with perfectly linear elastic bulk materials can reach unphysical levels (> 100 m/s), particularly for fault models with higher effective normal stress (e.g. $\overline{\sigma} = 100$ MPa). In real rocks, such high slip rates, and hence strain rates, would be mitigated by the onset of additional inelastic deformation around the rupture front, which is not explicitly included in the spectral boundary integral method that we use.

Numerical studies of dynamic rupture propagation with off-fault Drucker-Prager plasticity have shown that imposing a maximum slip velocity can mimic the effect of off-fault energy loss due to the plastic yielding of the off-fault materials under high strain rates[34]. In full consideration of plasticity, the yielding conditions depend upon the bulk material properties and confining conditions. For consistency and simplicity, here we employ a fixed value of $V_{\text{max}} = 15$ m/s, motivated by yielding considerations at a representative seismogenic depth of 10 km[34]. We have explored a range of maximum velocities in our simulations and found that the qualitative behavior of the resulting

ruptures, including the relationships among seismological parameters of interest, such as radiated energy, apparent stress, radiation efficiencies, stress drop, and average slip, do not substantially change for velocity limits of 10 m/s or above.

Interestingly, we find that the effect of mimicking the off-fault dissipation through the slip velocity limit is much larger for single ruptures with a given prestress than for ruptures in sequences of earthquakes and slow slip. Limiting slip velocities for single ruptures with the same prestress conditions can result in slower rupture propagation and diminished slip (Supplementary Fig. S19). In the context of sequences of events, however, the additional dissipation is balanced by ruptures nucleating at slightly higher average shear prestress in the cases that we have examined. This compensation, in turn, results in similar kinematics, such as average slip and stress drops, but mildly different energy partitioning (Supplementary Fig. S20). Simulations of single dynamic ruptures with the explicit incorporation of off-fault plasticity as well as enhanced dynamic weakening due to flash heating have also shown that the addition of off-fault plasticity increases the prestress levels at which self-healing pulses may occur[58]. In our simulations, we find that, following the first several events (Fig. 20), the average stress drop and slip tend to be comparable for simulations with and without the velocity limit, though the average breakdown energy and radiated energy differ. The initial weakening rate during ruptures is generally similar (Supplementary Fig. S20), but it is eventually slightly restricted by the velocity limit, leading to mildly larger G, which is expected with the incorporation of off-fault plasticity. However, while $\overline{\Delta\tau}$ is similar, $\overline{\tau}_{\text{ini}}$ and $\overline{\tau}_{\text{fin}}$ are both higher for ruptures including the velocity limit, though the dynamic level $\overline{\tau}_{\text{dyn}}$ is more or less the

same, resulting in a larger undershoot and therefore more radiated energy for the same static stress drop and slip (Supplementary Fig. S20).

These results highlight the importance of studying effects of off-fault plasticity on rupture propagation within the context of earthquake sequences where stress conditions evolve in a self-consistent manner based on previous slip events. Note that for much more stringent and perhaps unreasonable limits (e.g., $V_{\text{max}} = 1$ m/s) favor higher prestress conditions and predominantly crack-like rupture propagation. The specific effects of off-fault plasticity on rupture propagation and energy partitioning merits much more detailed study.

Reference to idealized crack model

In comparing local slip duration of crack-like and pulse-like ruptures (Fig 3 of the main text), we refer to the idealized case of a 2-D antiplane rupture expanding as a symmetric elliptical crack with constant rupture speed and stress drop, which has been extensively studied both analytically and numerically[31,89]. The rupture expands with constant rupture speed v_r to a crack half-length a, then abruptly arrests at $t = t^{\text{arr}} = \frac{a}{v_r}$, producing the slip profile[89]:

$$\delta_1(z, t^{\text{arr}}) = \frac{1}{E\left(\sqrt{1 - v_r^2/c_s^2}\right)} \frac{\Delta\tau}{\mu} \left(a^2 - z^2\right)^{1/2} \tag{S14}$$

where μ is the shear modulus, $\Delta\tau$ is the stress drop which is uniform over the rupture length, c_s is the shear wave speed, and E is the complete elliptic integral of the second kind. Following the abrupt arrest is a period of wave-mediated stress redistribution along with the propagation of healing waves from the ends of the rupture. This period of stress redistribution leads to an

adjustment of the final (static) slip profile to:

$$\delta_1(z, t^{\text{fin}}) = \frac{\Delta\tau}{\mu}\left(a^2 - z^2\right)^{1/2} \tag{S15}$$

The wave-mediated stress adjustment following rupture arrest results in a stress overshoot where the final stress is lower than the dynamic sliding level. This stress overshoot can vary from 15 percent at $v_r = 0.6c_s$ to about 20 percent at $v_r = 0.9c_s$ from the static solution[31].

After the abrupt arrest at the rupture boundary, slip continues within the center of the ruptured region until the arrival of healing waves propagating from the boundaries. Accounting for the propagation of healing waves, assumed to propagate at speed c_h, the total slip duration can be estimated as:

$$T = a\left(\frac{1}{v_r} + \frac{1}{c_h}\right) \tag{S16}$$

Similarly, the local sliding duration or rise time as a function of location can be estimated as,

$$t(x_3) = \left(\frac{1}{v_r} + \frac{1}{c_h}\right)(a - |z|) \tag{S17}$$

The spatial average of the rise time over the ruptured region is then,

$$\bar{t} = \frac{\left(\frac{1}{v_r} + \frac{1}{c_h}\right)\int_{-a}^{a}(a - |z|)dz}{2a} = \frac{a}{2}\left(\frac{1}{v_r} + \frac{1}{c_h}\right) \tag{S18}$$

giving the ratio $\bar{t}/T = 0.5$. Note that for similar considerations with a perfectly symmetric rupture in 3D the average rise time would be,

$$\bar{t} = \frac{\left(\frac{1}{v_r} + \frac{1}{c_h}\right)\int_0^{2\pi}\int_0^{a}(a - r)rdrd\theta}{\pi a^2} = \frac{a}{3}\left(\frac{1}{v_r} + \frac{1}{c_h}\right) \tag{S19}$$

with the same total duration T. The spatial average of the rise time is smaller in 3D given that a greater proportion of the rupture area consists of near-arrest portions of the rupture where slip durations are relatively short compared to the interior. In this case, the ratio of the average rise time to duration is $\bar{t}/T = 0.33$, which is a modest adjustment of the 2D solution.

Supplementary Text

Energy Budget for Earthquakes

The earthquake energy budget considers the partitioning of the total strain energy change ΔW into the dissipated energy, E_{Diss}, and the energy radiated away from the source region to the far-field, E_R:

$$\Delta W = E_{\text{Diss}} + E_R. \tag{S20}$$

This relation can also be written per unit source area as:

$$\Delta W/A = E_{\text{Diss}}/A + E_R/A \tag{S21}$$

The total strain energy change per unit area on the fault $\Delta W/A$ is given by[90]:

$$\Delta W/A = \frac{1}{2}(\bar{\tau}_{\text{ini}} + \bar{\tau}_{\text{fin}})\bar{\delta}, \tag{S22}$$

where $\bar{\tau}_{\text{ini}}$ is the average initial stress, $\bar{\tau}_{\text{fin}}$ is the average final stress, $\bar{\delta}$ is the average final slip, and where[35]:

$$\bar{\tau}_{\text{ini}} = \frac{\int_\Sigma \tau_{\text{ini}}(z)\delta_{\text{fin}}(z)dz}{\int_\Sigma \delta_{\text{fin}}(z)dz}, \tag{S23}$$

$$\bar{\tau}_{\text{fin}} = \frac{\int_\Sigma \tau_{\text{fin}}(z)\delta_{\text{fin}}(z)dz}{\int_\Sigma \delta_{\text{fin}}(z)dz}. \tag{S24}$$

In this study, we follow the work of Noda and Lapusta (2012)[35], which provides an averaging methodology for constructing the average shear stress vs. slip diagrams, $\overline{\tau}(\delta')$. The dissipated energy within the source volume can then be calculated by integrating the area under the average stress-slip curve in the energy diagram,

$$E_{\text{Diss}} = \int_0^{\overline{\delta}} \overline{\tau}(\delta') d\delta', \tag{S25}$$

and the energy that is radiated outside of the source region as seismic waves is determined by the difference between the strain energy change and dissipated energy within the volume,

$$E_R = \Delta W - E_{\text{Diss}}. \tag{S26}$$

While it is presumed that the radiated energy can be inferred from seismological observations[24,30,43,90–95], determining the total strain energy change and dissipated energy is challenging as it requires knowledge of the absolute stress levels throughout the source process. The dissipated energy is often partitioned further into the breakdown energy G[44,96] and the "frictionally dissipated" energy E_F/A. The breakdown energy G is thought to be the part of the dissipated energy that controls the dynamics of the rupture, often considered as the frictional analog of fracture energy from singular and cohesive-zone models of dynamic fracture theory. The so-called frictionally dissipated energy E_F is the remaining portion of the dissipated energy which is assumed to not affect the dynamics of the source process. Note that while the only source of dissipation in our simulations is through frictional resistance, natural shear ruptures can also experience contributions from dissipation within the surrounding volume, such as from the activation or production of damage during

ruptures. We partially approximate this effect by impose the velocity limit, as discussed in the Methods and Supplementary Materials.

The averaging methodology for the representative shear stress vs. slip evolution during dynamic rupture can serve as the energy partitioning diagram as it preserves the total event energy quantities such as strain energy change, dissipated energy and therefore radiated energy. However it does not necessarily precisely preserve the average breakdown energy. The true average breakdown energy can be defined as the spatial average of the local breakdown energy with respect to the local stress minima $\tau_{min}(x)$:

$$G = \frac{1}{A}\int_{\Sigma}\left[\int_{0}^{\delta(\tau_{\min(x)})} \tau(\delta) - \tau_{\min}(\delta)d\delta\right]dz \tag{S27}$$

which is how we compute the average breakdown energy in our models. This is not necessarily equivalent to the breakdown energy reflected in the average diagram, since the minimum shear stress of the average curve does not have a simple relation to the minima of the curves of each ruptured point. Numerical studies of crack-like ruptures including thermal pressurization found that these two averaged quantities give similar, but not identical results[28]. Therefore, the representation of G from the average energy diagram can illustrate the average breakdown energy but does not represent its exact value.

Standard Analysis of Earthquake Energy Balance

The standard earthquake energy analysis considers an idealized average stress vs. slip rupture model (Fig. 4 of the main text) in order to express energy-related quantities that are thought to be

relevant to the source dynamics in terms of potentially seismologically-inferable quantities, namely stress drop, average slip, and radiated energy. An important aspect of the analysis is the concept of "available energy," or the energy associated with the breakdown process and radiation, effectively the energy thought to be relevant to the dynamics of the earthquake rupture[24,30,43,90–92,94,95]. We can define the true available energy per unit area $\Delta W_0^{\text{true}}/A$ as the sum of the breakdown energy (defined per unit source area) and radiated energy per unit source area:

$$\Delta W_0^{\text{true}}/A = G + E_R/A. \tag{S28}$$

Given this definition, one can also compare the relative magnitudes of the breakdown and radiated energy through a quantity known as radiation efficiency[95]:

$$\eta_R^{\text{true}} = \frac{E_R/A}{G + E_R/A} = \frac{E_R/A}{\Delta W_0^{\text{true}}/A}, \tag{S29}$$

The determination of the available energy is fairly straight forward given the idealized energy diagram of Fig. 4[30,95,97]. In this idealized model, the shear stress evolution follows simplified linear slip weakening where stress drops linearly from an initial value $\overline{\tau}_{\text{ini}}$ until slip reaches a critical value D_c, at which the stress remains constant at $\overline{\tau}_{\text{dyn}}$ for the remainder of slip, with $\overline{\tau}_{\text{fin}} = \overline{\tau}_{\text{dyn}}$. The available energy in this case can be represented by:

$$\Delta W_0^{\text{inf}}/A = \frac{1}{2}\overline{\Delta\tau}\,\overline{\delta}, \tag{S30}$$

which we call the seismologically-inferable available energy, as it is based on quantities that can be inferred seismologically. Here $\overline{\delta}$ is the average slip and $\overline{\Delta\tau}$ is the energy-based stress drop [35,68]:

$$\overline{\Delta\tau} = \bar{\tau}_{\text{ini}} - \bar{\tau}_{\text{fin}} = \frac{\int_\Sigma \Delta\tau(z)\delta_{\text{fin}}(z)dz}{\int_\Sigma \delta_{\text{fin}}(z)dz}. \tag{S31}$$

Given this definition, one defines the seismologically-inferable radiation efficiency as:

$$\eta_R^{\text{inf}} = \frac{E_R}{\Delta W_0^{\text{inf}}/A} = \frac{E_R/A}{\frac{1}{2}\overline{\Delta\tau}\,\bar{\delta}}. \tag{S32}$$

This quantity can, and has been, estimated from seismological observations[24,95]. Note that while $0 \leq \eta_R^{\text{true}} \leq 1$ by definition, η_R^{inf} can in principle exceed 1. In that sense, η_R^{true} can be called a radiation efficiency but η_R^{inf} is more accurately a radiation ratio [68].

Within the context of the idealized rupture model represented by the standard energy diagram (Fig. 4), it can be seen that:

$$\Delta W_0^{\text{inf}}/A \;\equiv \frac{1}{2}\overline{\Delta\tau}\,\bar{\delta} \;=\; \Delta W - E_F \;=\; E_R/A + G \equiv \Delta W_0^{\text{true}}/A \tag{S33}$$

Given this notion of available energy, there have also been attempts to estimate the average breakdown energy G for natural earthquakes based on $\Delta W_0^{\text{inf}}/A$ and E_R/A[6,24,26]. Assuming relations equivalent to the standard energy diagram, one can subtract the radiated energy E_R/A from the seismologically-inferred available energy $\Delta W_0^{\text{inf}}/A$, thus leading to the seismologically-estimated breakdown energy G^{inf}:

$$G^{\text{inf}} = \Delta W_0^{\text{inf}}/A - E_R/A. \tag{S34}$$

Substituting values that can be inferred seismologically, we can define the inferable quantity[6,26]:

$$G' = \frac{1}{2}\bar{\delta}\left(\overline{\Delta\tau} - \frac{2\mu E_R}{M_0}\right), \tag{S35}$$

where μ is the shear modulus and M_0 is the seismic moment of the event. The last term is proportional to the apparent stress, $\sigma_A = \mu\frac{E_R}{M_0}$[98].

Discrepancy between dynamic fault resistance and final post-earthquake stress: consequences for estimating energy-related quantities

In our simulations, the final average shear stress is typically not the same as the dynamic level of shear stress, which is a potential issue with the standard energy analysis. This mismatch is due to either a dynamic stress undershoot, as typical for self-healing pulses, or a dynamic stress overshoot, as often the case for crack-like ruptures (Supplementary Fig. S2)[27,30,99]. Note that the two levels of stress are not expected to be linked physically, since the dynamic shear resistance is determined by a host of mechanisms acting during slip, such as rate-and-state friction, shear heating, fluid effects, etc, while the final static stress depends only on the initial stress and the final static slip.

The discrepancy between the final stress and dynamic fault resistance can significantly affect the considerations of the earthquake energy balance. Here, we consider a few relevant simple modifications of the standard energy diagram and the resulting relationship between the inferable and true available energies, ΔW_0^{inf} and ΔW_0^{true}, respectively. Recall that the frictionally dissipated energy E_F is defined as the energy dissipated below the lowest average dynamic level of shear stress $\overline{\tau}_{\text{dyn}}$ in the average stress vs. slip diagram. We can define an alternative form of the true available energy $\Delta \hat{W}_0^{\text{true}}$ based on the average stress vs. slip diagram:

$$\Delta \hat{W}_0^{\text{true}}/A = \Delta W/A - E_F/A = \frac{1}{2}(\bar{\tau}_{\text{ini}} + \bar{\tau}_{\text{fin}})\bar{\delta} - \bar{\tau}_{\text{dyn}}\bar{\delta}. \tag{S36}$$

Note that this expression for the true available energy is not necessarily the same as the previous definition $\Delta W_0^{\text{true}}/A \equiv E_R/A + G$, as mentioned earlier due to the complicated relationship

between the minimum of the average curve and the average of the local stress-slip curves which provide G. In addition, the relationship assumes that the fault does not recover appreciably from the minimum level of average dynamic stress before the final slip. Additional energy may be dissipated after the rupture reaches its minimum dynamic level of stress if it restrengthens with slip rather than only at the final slip. In our simulations we find that this effect is normally negligible compared to the other energy quantities and $\Delta\hat{W}_0^{\text{true}} \approx \Delta W_0^{\text{true}}$.

If the rupture behavior includes a stress undershoot of size $\gamma\overline{\Delta\tau}$, as occurs in self-healing pulse-like ruptures, $\Delta\hat{W}_0^{\text{true}}$ may be written in terms of $\gamma\overline{\Delta\tau}$ and ΔW_0^{inf}:

$$\begin{aligned}\Delta\hat{W}_0^{\text{true}}/A &= \frac{1}{2}\overline{\Delta\tau}\bar{\delta} + (\bar{\tau}_{\text{fin}} - \bar{\tau}_{\text{dyn}})\bar{\delta} \\ &= \Delta W_0^{\text{inf}}/A + \gamma\overline{\Delta\tau}\bar{\delta}.\end{aligned} \tag{S37}$$

We see then that the ratio between the true and seismologically-inferable available energies depends on the extent of the over- or undershoot:

$$\frac{\Delta\hat{W}_0^{\text{true}}}{\Delta W_0^{\text{inf}}} = 1 + 2\gamma. \tag{S38}$$

If $\gamma = 0$, we have the idealized case and $\Delta\hat{W}_0^{\text{true}} = \Delta W_0^{\text{inf}}$. If there is a non-negligible undershoot, then $\gamma > 0$ and $\Delta\hat{W}_0^{\text{true}} > \Delta W_0^{\text{inf}}$. The ratio between the true and seismologically-inferable available energies can also be expressed as the ratio between η_R^{inf} and η_R^{true} (Supplementary Fig. S21):

$$\frac{\Delta\hat{W}_0^{\text{true}}}{\Delta W_0^{\text{inf}}} = \frac{E_R/A + G}{\frac{1}{2}\overline{\Delta\tau}\,\bar{\delta}} = \frac{\eta_R^{\text{inf}}}{\eta_R^{\text{true}}} \tag{S39}$$

Note that, for rupture behavior with a non-zero increase from $\overline{\tau}_{\text{ini}}$ to $\overline{\tau}_{\text{peak}}$ (called strength excess), the additional dissipated energy does not alter the available energy. This initial increase affects how available energy is partitioned into breakdown energy G and radiated energy E_R/A, but does not change the actual available energy ΔW_0^{true} of the rupture. The strength excess increases the breakdown energy G at the expense of radiated energy E_R/A.

The same argument can be made for rupture behaviors with an overshoot as is often the case with crack-like ruptures, and equation (S37) still applies, with negative values of γ. This behavior would result in $\Delta\hat{W}_0^{\text{true}} < \Delta W_0^{\text{inf}}$ but, in most simulations, $|\gamma| \ll 1$ for crack-like ruptures, and thus $\Delta W_0^{\text{true}} \approx \Delta W_0^{\text{inf}}$. Numerical studies have shown that the seismologically estimated breakdown energy G^{inf} agrees well (within a factor of 2) with the true breakdown energy G for crack-like events incorporating thermal pressurization[28], which is consistent with the simulations in this study (Supplementary Fig. S13).

As we have seen, if the fault experiences a substantial stress undershoot, the available energy for radiation and breakdown would be significantly underestimated. Let us consider the case where the fault experiences a stress undershoot of magnitude $\gamma\overline{\Delta\tau}$ and we can approximate the breakdown energy as $G \approx \frac{1}{2}(1+\gamma)\,\overline{\Delta\tau} D_c$. Then:

$$\begin{aligned} E_R/A &= \Delta\hat{W}_0^{\text{true}}/A - G \\ &= \frac{1}{2}\overline{\Delta\tau}\bar{\delta} + \gamma\overline{\Delta\tau}\bar{\delta} - \frac{1}{2}(1+\gamma)\overline{\Delta\tau} D_c, \end{aligned} \tag{S40}$$

$$\eta_R^{\text{inf}} = \frac{E_R}{\Delta W_0^{\text{inf}}/A} = 1 + 2\gamma - (1+\gamma)D_c/\bar{\delta}. \tag{S41}$$

Thus, E_R will exceed ΔW_0^{inf} for any undershoot such that:

$$\gamma > \frac{D_c/\bar{\delta}}{2 - D_c/\bar{\delta}}, \tag{S42}$$

which would lead to inferable radiation efficiencies (more appropriately called ratios) of $\eta_R^{\text{inf}} > 1$. If $\gamma > 1$, meaning that the undershoot is larger than the average stress drop, then the stress undershoot is large enough that E_R/A would always exceed ΔW_0^{inf}, no matter the slip-weakening distance D_c. If $\Delta W_0^{\text{inf}} \approx \Delta W_0^{\text{true}}$, as is the case for crack-like ruptures, then $\eta_R^{\text{inf}} \approx \eta_R^{\text{true}}$. However, for a substantial undershoot, as is the case for self-healing pulse-like ruptures, one would expect $\eta_R^{\text{inf}} \gg \eta_R^{\text{true}}$.

Notice that G^{inf} is also directly related to η_R^{inf}:

$$G^{\text{inf}} = \Delta W_0^{\text{inf}}/A - E_R/A \rightarrow \frac{G^{\text{inf}}}{\Delta W_0^{\text{inf}}/A} = 1 - \eta_R^{\text{inf}} \tag{S43}$$

Hence, if ΔW_0^{inf} underestimates ΔW_0^{true}, and we still subtract off E_R/A, then we are left with a significant underestimation of the true breakdown energy G. Indeed, in the case of substantial undershoot, $\gamma > 0.5$, the radiated energy can exceed ΔW_0^{inf}, therefore estimates of G^{inf} will also be negative (Figure 4c of main text), which is physically inconsistent with the concept of breakdown energy.

There is no simple way to calculate G reliably for self-healing pulse-like ruptures using current seismological observations. One approach has considered the case of a stress undershoot and

additionally assumed a complete coseismic stress loss ($\overline{\tau} = 0$) during large pulse-like events[27]. In that work, G_{max} is defined as:

$$G_{\text{max}} = G^{\text{inf}} + \bar{\tau}_{\text{fin}}\bar{\delta} = \frac{1}{2}\bar{\delta}\left(\overline{\Delta\tau} - \frac{2\mu E_R}{M_0}\right) + \bar{\tau}_{\text{fin}}\bar{\delta}. \tag{S44}$$

To calculate G_{max}, the absolute final stress on the fault must be known (or assumed) and the dynamic level of stress is assumed to be zero, thereby assuming that the available energy is the total strain energy change. This metric assumes that all of the dissipated energy is incorporated into the breakdown energy, hence it represents the maximum potential breakdown energy given the assumed absolute stress levels. Note that G_{max} can dramatically overestimate G if the fault does not weaken to zero strength.

Discrepancy between dynamic fault resistance and final post-earthquake stress: consequences for apparent stress

The existence of stress undershoot/overshoot also affects the interpretation of apparent stress. A number of seismological studies have associated variations in apparent stress with differences in static stress drop[25,37,38,99]. We can approximate the relationship between apparent stress and static stress drop by dividing equation (S40) by average slip:

$$\sigma_A = \frac{E_R}{\bar{\delta}A} = \overline{\Delta\tau}\left[\frac{1+2\gamma}{2} - \frac{1+\gamma}{2}\frac{D_c}{\bar{\delta}}\right]. \tag{S45}$$

This relation shows that increasing static stress drop $\overline{\Delta\tau}$ indeed leads to increasing apparent stress, for the same γ and $D_c/\bar{\delta}$. However, even if two ruptures have comparable static stress drop, the apparent stress would considerably differ if the two ruptures exhibit different undershoot/overshoot. For the idealized case with no substantial undershoot ($\gamma = 0$), $\sigma_A \approx \overline{\Delta\tau}\left[1/2 - D_c/2\bar{\delta}\right]$, whereas

for an undershoot of $\gamma = 1$, $\sigma_A \approx \overline{\Delta\tau}\left[3/2 - D_c/\overline{\delta}\right]$. Assuming again that D_c is similar for the two cases, this would result in over a factor of 3 greater apparent stress for the undershoot of $\gamma = 1$. For $\gamma = 2$, this increases to at least a factor of 5.

Our simulations indeed show that the ratio of radiated energy to moment, and thus apparent stress, increases for both increasing static stress drop and undershoot (Supplementary Fig. S3). In fact, ruptures with smaller static stress drops but considerable undershoot can have higher apparent stress than ruptures with larger static stress drops but mild to no undershoot. For example, if we examine crack-like ruptures and self-healing pulses in models with the same quasi-static strength, our simulated self-healing pulses tend to have smaller average static stress drops but higher ratios of radiated energy to moment in comparison to simulated crack-like ruptures (Supplementary Fig. S12).

As the apparent stress is sensitive to both the static stress drop and degree of undershoot, according to our simulations, a (relatively high) radiated energy to moment ratio around 10^{-4} may be indicative of either a moderately sharp self-healing pulse with a standard stress drop around 2 - 3 MPa and undershoot $\gamma \approx 1.5$, or a crack-like rupture with negligble undershoot/overshoot and a larger stress drop of 10 - 15 MPa. The seismologically-inferable radiation efficiency scales the radiated energy by both the potency $\overline{\delta}A$ and static stress drop $\overline{\Delta\tau}$, resulting in a single scalar quantity that may provide insight into the degree of stress undershoot and rupture style. While the inferable radiation efficiency is not a true efficiency, it describes a scaled energy measure with

reference to an idealized fracture model, providing a useful metric for how compatible the average source process is with a crack-like rupture (Fig. 3A and S4). Note that the discussed relationships between radiated energy, moment, static stress drop, and average slip depend on stress changes during the rupture but not the absolute stress levels (Supplementary Fig. S3-5).

The relationship between apparent stress, stress undershoot and static stress drop emphasizes the need for improving constraints on static stress drops from large earthquakes. For example, apparent stress is inferred to be systematically higher for intraplate earthquakes, which also are typically inferred to have higher static stress drops[23,36,37]. The apparent stress is sometimes used as a constraint for inversions of static stress drop, where it is assumed that the static stress drop must be larger than the apparent stress, consistent with a stress overshoot for crack-like ruptures[45,100]. The uncertainty of stress drops can be quite high; for example a Mw 6.5 intraplate earthquake offshore Northern California in 2010 has been inferred static stress drops between 2 and 20 MPa, with a high value of apparent stress around 7 MPa[100]. Note that the 7 MPa apparent stress with a lower-end estimate of static stress drop at 2 MPa results in a seismologically-inferable radiation efficiency (or radiation ratio) around 3, consistent with our relatively sharp simulated self-healing pulses and considerable undershoot. However, if the apparent stress is lower than the static stress drop, then the radiation ratio would be less than 1, consistent with crack-like ruptures and dynamic overshoot.

Radiated energy from self-healing pulses: relation to local rupture behavior, qualitative consistency for different rupture arrest and for longer faults

The average stress-slip curves that we produce for our ruptures, including pulse-like, are representative of typical local behavior (Figs. S5 and S16). At the same time, the simulated pulses in this study are not steady but exhibit variations in local slip, slip rate, and rupture speed, resulting in seismic radiation and non-zero local static stress changes throughout the rupture process (Supplementary Figs. S5-6). Hence our simulated slip pulses are quite different from the theoretical case of an infinitely propagating steady pulse in which all the total strain energy change is dissipated within the source region, implying no net radiated energy. Note, however, that there is no notion of far-field radiation for an infinite fault given that the entire infinite domain is the source region. Moreover, the relevance of the infinitely propagating steady pulse model for natural earthquakes is not readily apparent, as not only the radiated energy but also static stress drop are zero for such models[46]. Several theoretical and numerical studies have examined such steady pulse propagation and shown that it is highly unstable, with pulses eventually dying or growing as a result of small perturbations in prestress[101,102].

To study the effect of rupture nucleation and arrest on the radiated energy, we conduct simulations with different properties of the VS regions that surround our seismogenic region. Modifying the VS properties modifies the nucleation process as well as allows for smoother or more forcible arrest. We find that models with significantly different properties of the arresting regions produce qualitatively similar results for the radiated energy per moment (Supplementary Fig. S22).

Our simulations are performed with a 24-km velocity-weakening region due to computational limitations, given the long simulations to generate long earthquake sequences and resolution required for such simulations with efficient enhanced weakening. The conclusions should hold for a longer fault as well, as we illustrate by considering a twice longer, 50-km velocity-weakening region (Supplementary Figs. S7 and S23). In general, while the specific values of the average source properties such as average stress drop, slip, radiated energy and average breakdown energy may vary based on the geometry and properties of the fault, the main findings presented in this study should be qualitatively consistent, in that any conditions that result in an average stress undershoot, or larger average dynamic stress changes than static stress changes, would result in higher radiated energy for the same average slip and static stress drop.

On crack-like vs. pulse-like ruptures

We find that self-healing pulses require higher average prestress than crack-like ruptures to achieve the same average dynamic stress levels and static stress drops. Crack-like ruptures within our simulations experience relatively minor under/overshoot with respect to their static stress drop, therefore the average initial stress in the rupture area is around one static stress drop away from the average dynamic resistance level:

$$\overline{\tau}_{\text{ini}} \approx \overline{\tau}_{\text{dyn}} + \overline{\Delta\tau}. \tag{S46}$$

In contrast, self-healing pulse-like ruptures experience a substantial undershoot γ, such that the average initial stress is significantly more than one stress drop away from the average dynamic resistance level:

$$\overline{\tau}_{\text{ini}} = \overline{\tau}_{\text{dyn}} + (1+\gamma)\overline{\Delta\tau}. \tag{S47}$$

where $\gamma \geq 0.5$. Therefore, self-healing pulses have higher average prestress than crack-like ruptures, for the same average dynamic stress levels and static stress drops. This consideration implies a minimum average initial stress that is needed for self-healing pulses; if we take $\overline{\tau}_{\text{dyn}} = 0$ MPa as the minimum dynamic stress level, then the minimum average initial stress for a self-healing pulse is $\overline{\tau}_{\text{ini}}^{\text{min}} = (1+\gamma)\overline{\Delta\tau}$. So for a minimum stress drop of 1 MPa, the average initial stress must be $\overline{\tau}_{\text{ini}} \geq (1+\gamma)$ MPa.

Another implication is that crack-like ruptures have larger stress drops than self-healing pulses, for the same average initial stress and dynamic stress levels (Supplementary Fig. S23). This is because $\overline{\Delta\tau}^{\text{ pulse}} = \left(\overline{\tau}_{\text{ini}} - \overline{\tau}_{\text{dyn}}\right)/(1+\gamma)$, whereas $\overline{\Delta\tau}^{\text{ crack}} \approx \overline{\tau}_{\text{ini}} - \overline{\tau}_{\text{dyn}}$, resulting in the relation,

$$\overline{\Delta\tau}^{\text{ crack}} \approx (1+\gamma)\overline{\Delta\tau}^{\text{ pulse}}, \tag{S48}$$

given the same average initial and dynamic stress levels. It is then apparent that the crack-like ruptures must have lower average initial stress for crack-like ruptures and self-healing pulse-like ruptures to have similar average dynamic stress levels and static stress drops.

Note that all ruptures nucleate in regions of relatively high stress, close the the quasi-static strength (Supplementary Fig. S1). However, enhanced weakening allows for larger dynamic stress changes at the rupture front which facilitates rupture propagation over regions of the fault with lower prestress. In the case of persistently weak faults, the stress changes at the rupture front are more mild, requiring prestress levels to be not too far from the quasi-static strength for the rupture to propagate (Supplementary Fig. S1B).

We find that fault models with high quasi-static strength and ultra-efficient dynamic weakening can support crack-like ruptures at fairly low levels of shear prestress, in which case they can have reasonable stress drops. The reasoning is as follows. Theoretical and numerical studies have shown that ruptures can take the form of self-healing pulses, provided that the background shear stress is around or below a critical stress level τ^{pulse} that depends on the properties of dynamic weakening [22,103]. In other words, there exists a critical background stress level τ^{pulse}, below which, if a rupture is to propagate, it can only propagate as a self-healing pulse. As the efficiency of the weakening increases, τ^{pulse} decreases. Hence if the weakening is quite efficient, then τ^{pulse} can be near-zero, and crack-like ruptures may be able to propagate at fairly low levels of shear stress (even though the levels would have to be higher than τ^{pulse}).

Let us consider a fault model (Model A) with an effective confining stress of 100 MPa and efficient thermal pressurization ($\Lambda = 0.34$ MPa/K and $\alpha_{hy} = 10^{-3}$ m^2/s), resulting in self-healing pulses. Now consider another fault model (Model B) with similar physical conditions, except with more efficient thermal pressurization ($\Lambda = 0.5$ MPa/K and $\alpha_{hy} = 10^{-6}$ m^2/s). In such conditions, the crack-like rupture in Model B is able to propagate with an average initial stress that is even lower than the self-healing pulse in Model A (Supplementary Fig. S8), with both ruptures propagating through average prestress well below the quasi-static strength ($\sim$70 MPa), and therefore consistent with (H1) quasi-statically strong but dynamically weak fault operation. Both ruptures experience large dynamic stress changes at the rupture front, increasing to peak stress levels around 100 MPa, and then dramatically weakening to shear resistance levels around or below

10 MPa due to thermal pressurization. The self-healing pulse dramatically weakens and then heals such that the static stress change is much smaller than the dynamic stress change (Supplementary Fig. S9). In contrast, the local shear stress within the crack-like rupture drops dramatically and stays low, with comparable local static and dynamic stress changes (Supplementary Fig. S9). The two ruptures have comparable static stress drops and average slip, and are compatible with (H1), operating at sliding resistance levels well below the same quasi-static strength. However, the self-healing pulse results in a substantial stress undershoot and therefore radiates considerably more energy, whereas the radiated energy for the crack-like rupture in Model B is comparable to those of milder crack-like ruptures with similar stress drop and slip, as well as seismological inferences.

While this example illustrates that the propagation of crack-like ruptures at stress levels much lower than the quasi-static strength is theoretically possible, the physical plausibility of such mechanism on natural faults is a topic for further exploration. In particular, such behavior would require substantially more efficient enhanced weakening than typically considered[6,13,32,57], which may be potentially suppressed, for example by the evolution of rock permeability or energy loss from damage production, during dynamic rupture.

One implication of the possibility for crack-like ruptures with efficient enhanced weakening propagating on quasi-statically strong, but dynamically weak faults is that they may exhibit comparable average source properties, such as static stress drops, average slip, radiated energy, apparent stress and seismologically inferable breakdown energies, as more mild crack-like ruptures

on persistently weak faults (Fig. 2D vs. Supplementary Fig. S8D). This poses a challenge for discriminating the local physical behavior of natural earthquakes from more remote teleseismic observations alone. However, the larger dynamic stress changes near the rupture front for both self-healing pulse-like ruptures and crack-like ruptures with efficient enhanced weakening would likely result in stronger near-fault ground motion (Supplementary Figs. S10A and S11). Indeed, the fault-parallel particle acceleration spectral amplitudes near the center of these ruptures on quasi-statically strong, dynamically weak faults in our models can be about a factor of 5 times those for the milder crack-like rupture on a persistently weak fault between 1 - 10 Hz (Fig. 9B). Note that high-frequency motions may also be considerably damped by the presence of off-fault inelastic deformation (Supplementary Fig. S10 B and Fig. S11 C-D) and attenuation, as well as enhanced by the presence of strong heterogeneities in both the rupture process and elastic bulk[58,104]. The expected near-fault ground motions from models with varying degrees of efficiency in enhanced weakening and rupture styles warrants more detailed study.

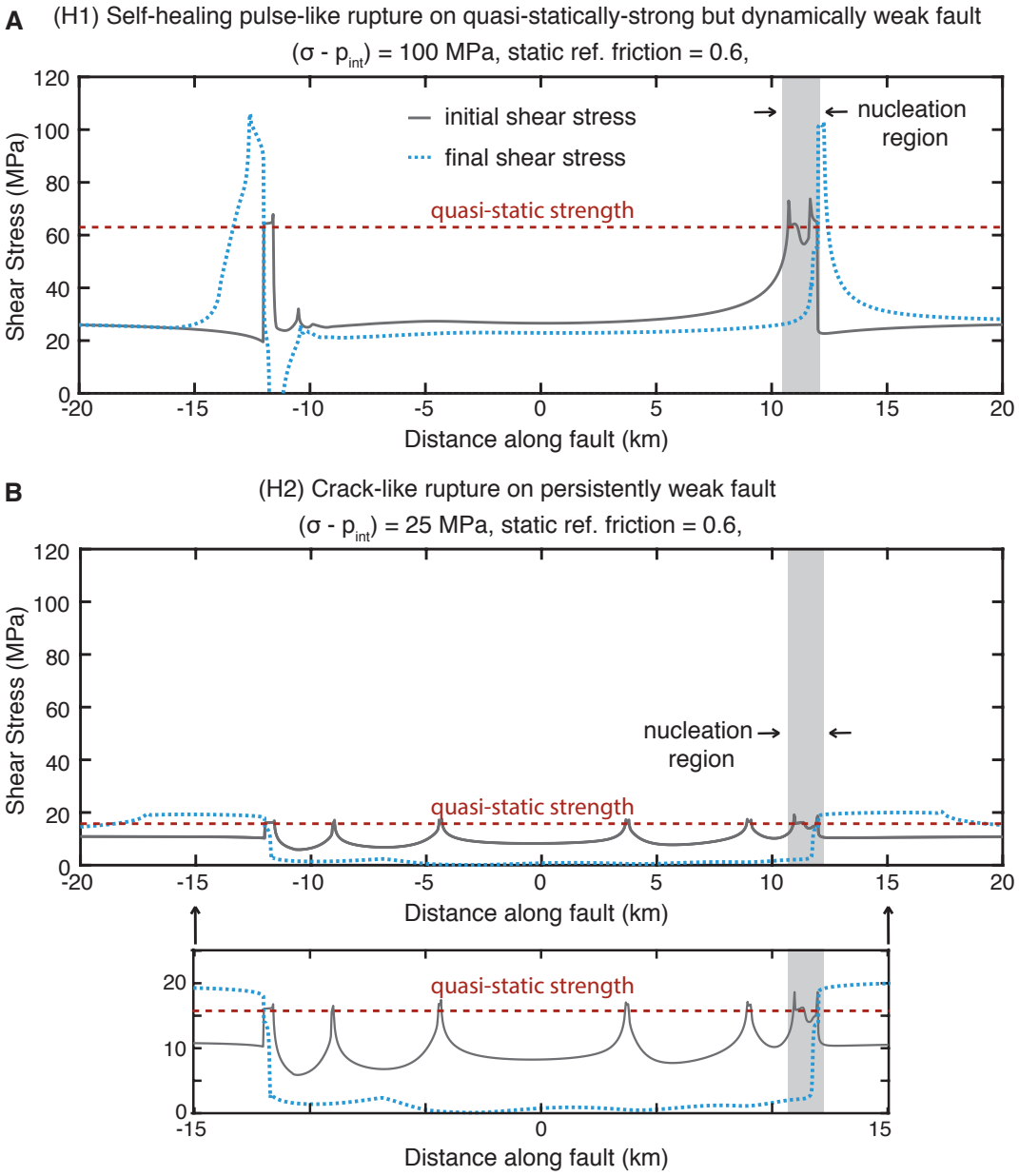

Fig. S1: Stress distributions before and after dynamic rupture for models of low-stress, low heat fault operation. Distribution of the initial (grey) and final (blue) shear stress along the fault for (A) a self-healing pulse-like rupture on a (H1) quasi-statically strong but dynamically weak fault, and (B) a crack-like rupture on a (H2) persistently weak fault. Both ruptures have similar average static stress drops around 7-8 MPa, and nucleate in a region with stress levels close to their respective quasi-static strength (grey bar). For the self-healing pulse (A), most of the fault is far below the quasi-static strength, whereas for the crack-like rupture the entire rupture region is within 1-2 times the static stress drop from the quasi-static strength.

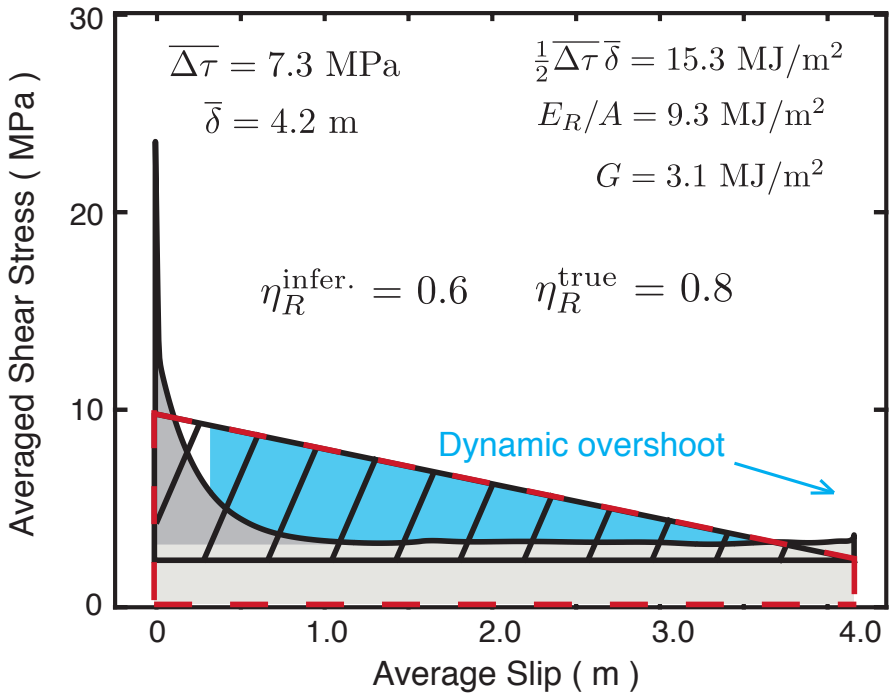

584

585 **Fig. S2: Average shear stress versus slip for a representative crack-like rupture (same as**
586 **Figure 2D but on enlarged scale)**. The average shear stress versus slip curve also serves as
587 the energy partitioning diagram for the crack-like rupture. Crack-like ruptures typically exhibit a
588 mild dynamic overshoot where the final average shear stress is lower than the average dynamic
589 resistance.

590

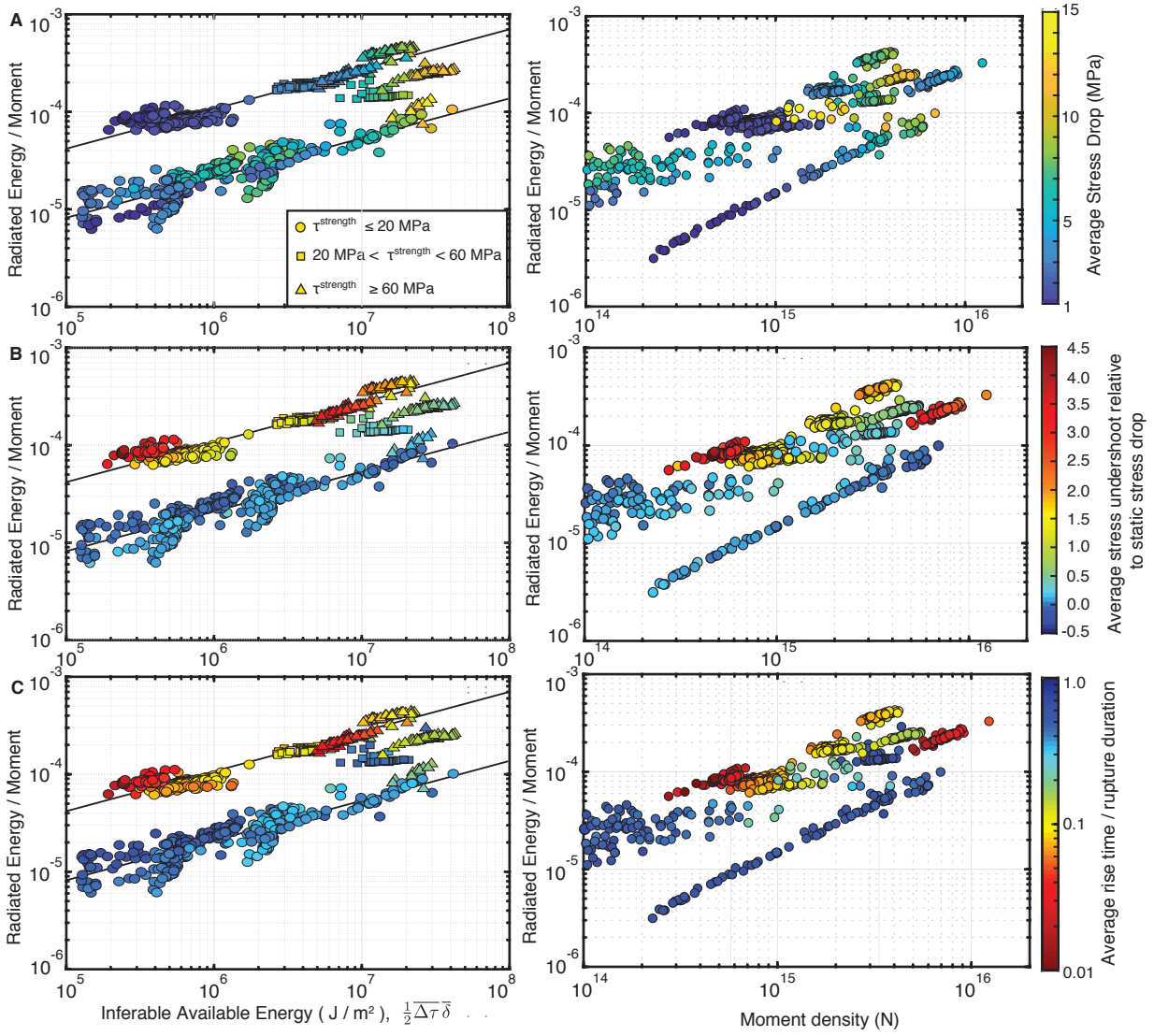

Fig. S3. Relationship between radiated energy, seismic moment, static stress drop and stress undershoot. (Left) Ratio of radiated energy to moment versus seismologically inferable available energy for simulated ruptures. Circles indicate models with average quasi-static strength τ^{strength} below 20 MPa, squares indicate those with τ^{strength} between 20 and 60 MPa and triangles indicate models with τ^{strength} greater than 60 MPa. (Right) Radiated energy to moment ratio versus 2D moment density for simulated ruptures. Ruptures are colored by A) average static stress drop, B) average stress undershoot, and C) the ratio of the average rise time to rupture duration.

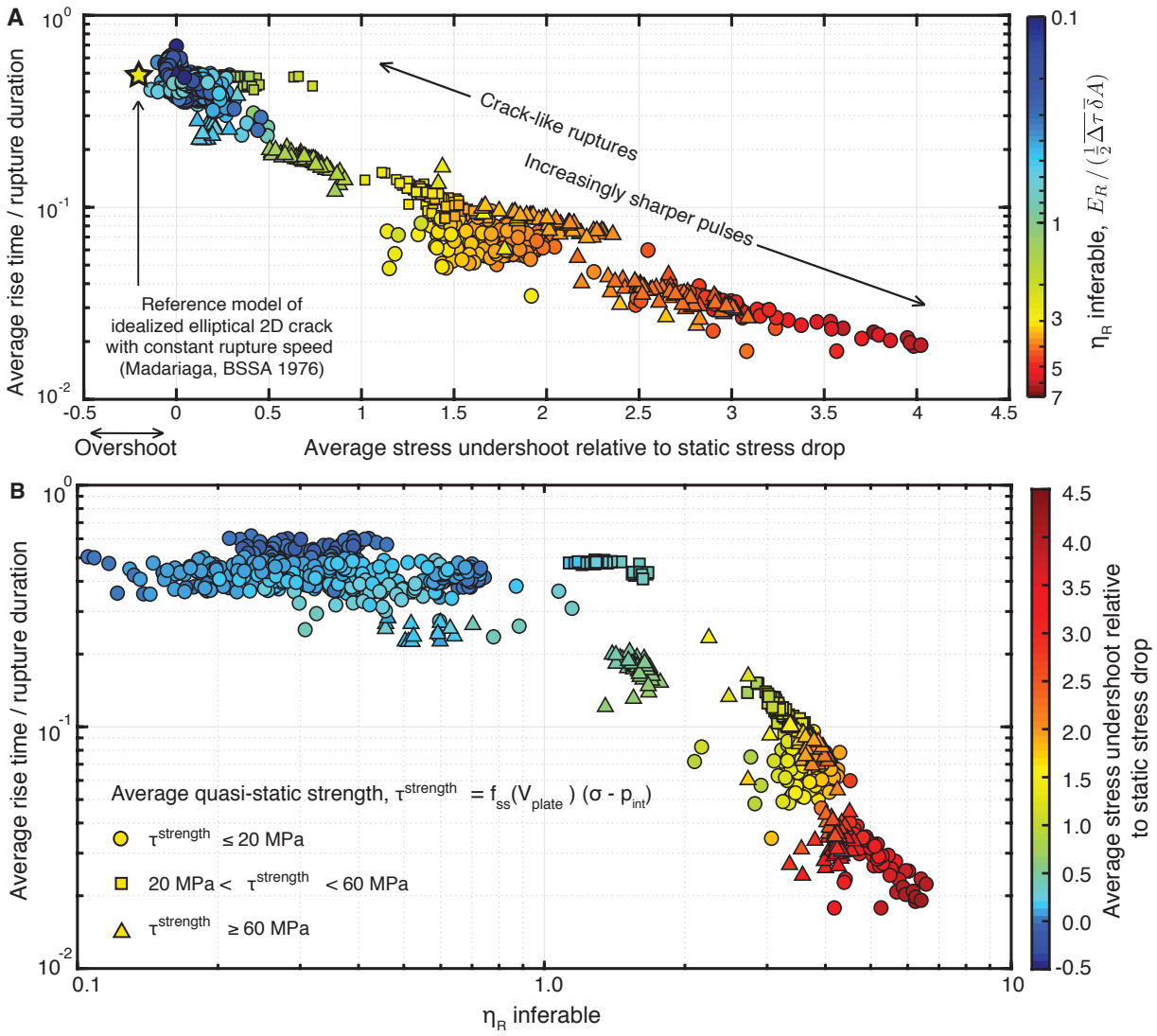

599

600 **Fig. S4. The relationship between rupture mode and inferable radiation efficiency.** (A)
601 The relationship between inferable radiation efficiency and undershoot does not depend on the
602 absolute stress levels. Circles indicate models with average quasi-static strength τ^{strength} below 20
603 MPa, squares indicate those with τ^{strength} between 20 and 60 MPa and triangles indicate models
604 with τ^{strength} greater than 60 MPa. B) Our simulated crack-like ruptures result in inferable radiation
605 efficiencies between 0.1 and 1.0, whereas self-healing pulses produce radiation efficiencies greater
606 then 1.

607

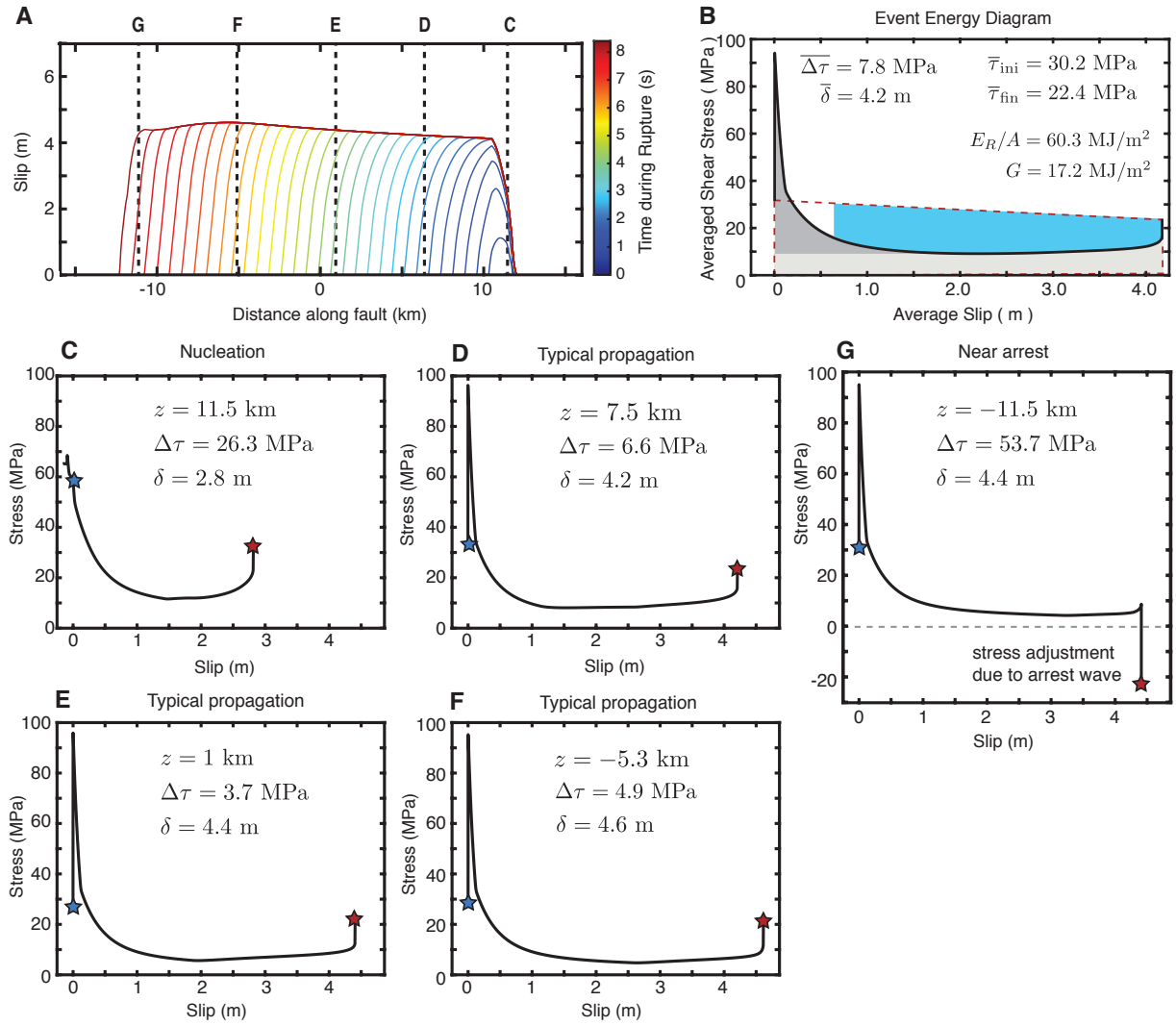

608

609 **Fig S5: Relationship between local and average stress versus slip behavior for a self-healing**
610 **pulse.** (A) Evolution of accumulated slip during a representative self-healing pulse-like rupture
611 with thermal pressurization TP1. Slip is contoured every 0.25 s. (B) Average shear stress vs. slip
612 behavior. The local behavior in all ruptures is variable, however we use the averaging methodology
613 of Noda and Lapusta (2012) to construct the average shear stress vs. slip behavior and illustrate
614 averaged source parameters. (C-G) The local evolution of shear stress with slip at five different
615 points throughout the rupture.

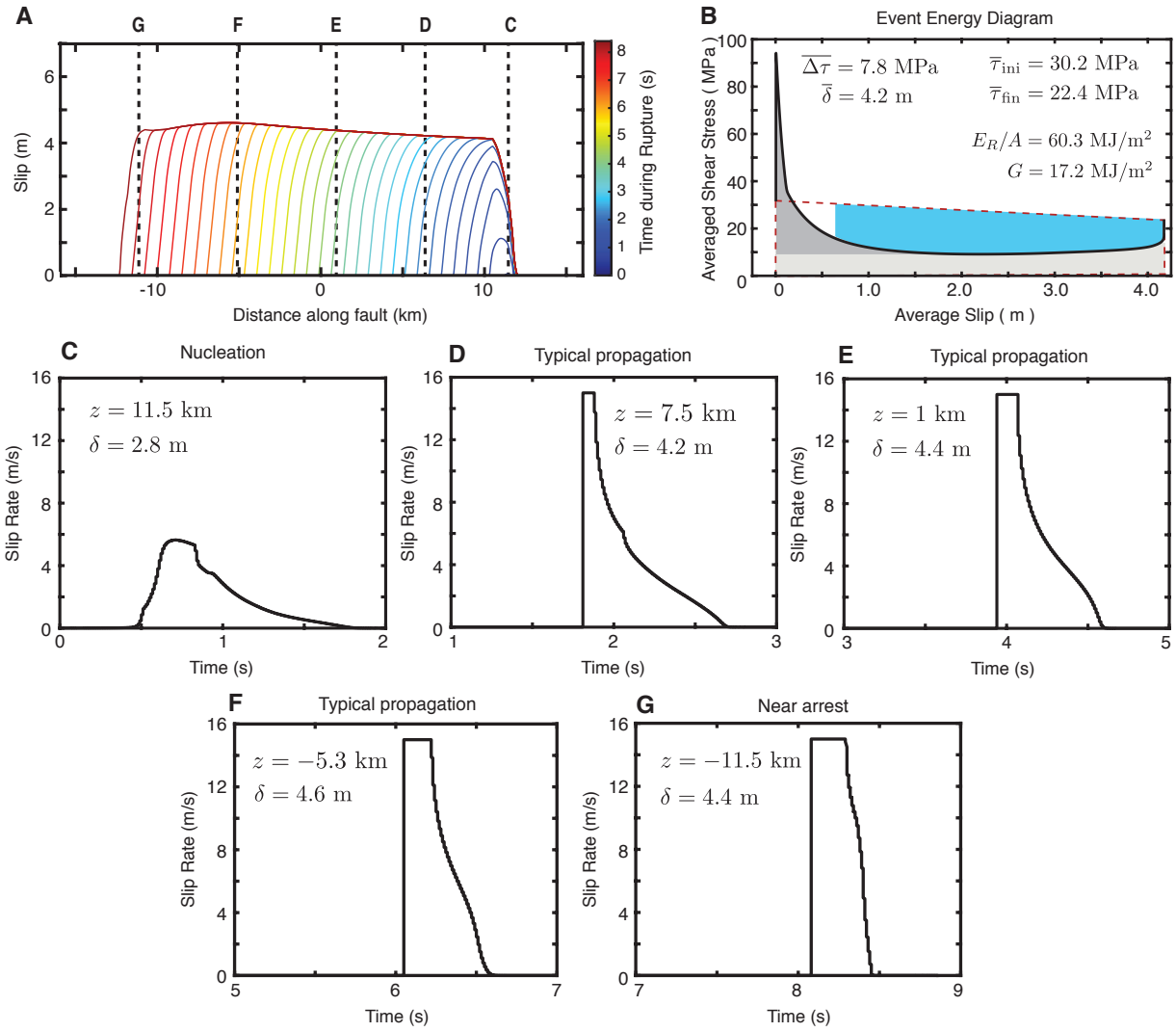

Fig S6: Evolution of slip pulse throughout the rupture process. (A) Evolution of accumulated slip during a representative self-healing pulse-like rupture with thermal pressurization TP1. Slip is contoured every 0.25 s. (B) Average shear stress vs. slip behavior. (C-G) The local evolution of slip rate with time at five different points throughout the rupture indicating the development of pulse and non-steady local behavior. As the rupture accelerates the pulse becomes sharper, with shorter local slip duration compared to the total rupture duration.

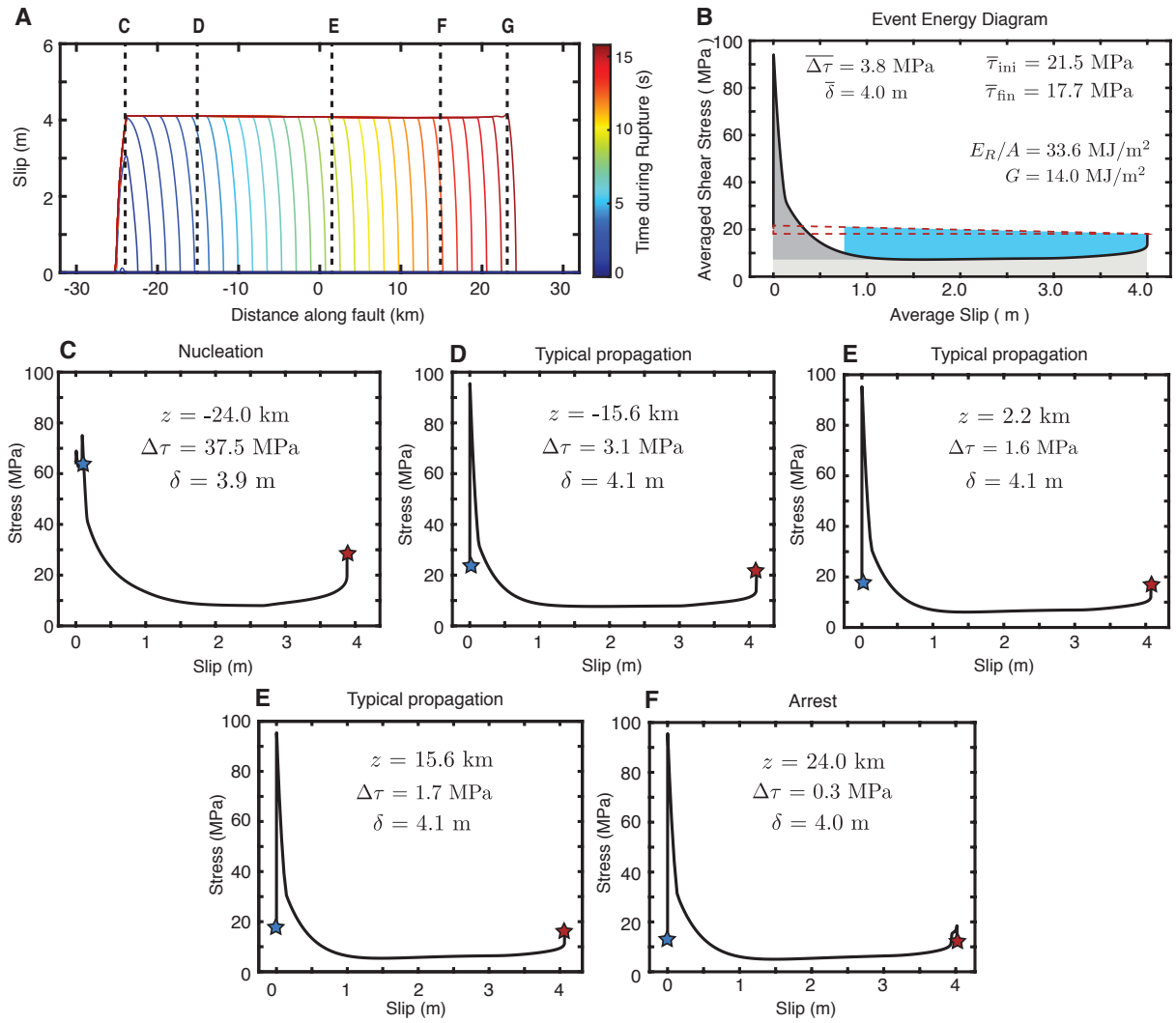

623

624 **Fig S7: Relationship between local and average stress versus slip behavior for a self-healing**
625 **pulse on a longer fault.** (A) Evolution of accumulated slip during a representative self-healing
626 pulse-like rupture with thermal pressurization TP1 on a longer fault with a 50-km VW region.
627 Slip is contoured every 0.5 s. (B) Average shear stress vs. slip behavior. The local behavior in
628 all ruptures is variable, however we use the averaging methodology of (Noda and Lapusta, 2012)
629 to construct the average shear stress vs. slip behavior and illustrate averaged source parameters.
630 (C-E) The local evolution of shear stress with slip at five different points throughout the rupture.
631 The general behavior is qualitatively similar to the self-healing pulses with similar properties on
632 the shorter fault with a 24-km VW region.

633

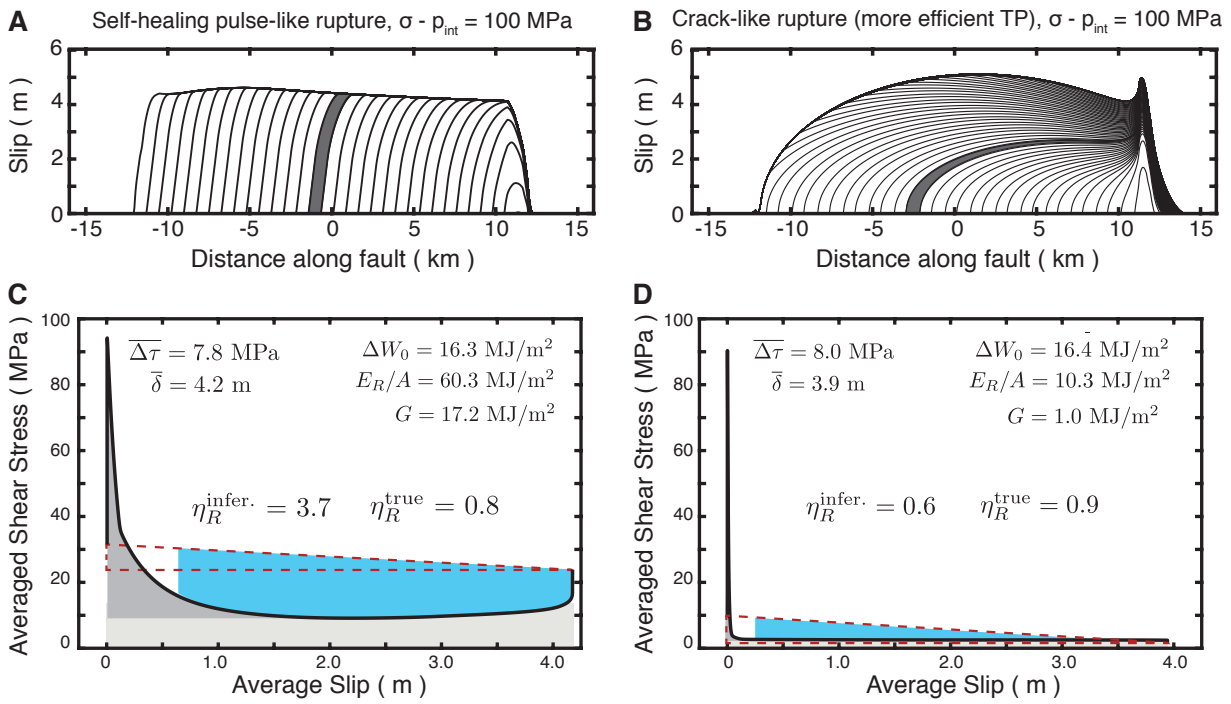

634

635 **Fig. S8: Energy partitioning for self-healing pulse and ultra-enhanced-weakening crack-**
636 **like rupture.** (A-B) Evolution of slip along the fault for a self-healing pulse-like rupture (A)
637 and crack-like rupture (B) with more efficient enhanced weakening. Contours are plotted every
638 0.25 s and the gray shading illustrates a portion of the fault that is slipping during a 0.25-second
639 interval. (C-D) The corresponding average evolution of shear stress vs. slip illustrating the radiated
640 energy (blue shading), as well as the dissipated energy, which is further separated into the average
641 breakdown energy (dark gray shading) and residual dissipated energy (light gray shading). The
642 seismologically-inferable available energy (red-dashed triangle) illustrates that the two ruptures
643 have similar static stress drop and average slip. The crack-like rupture with efficient enhanced
644 weakening experiences large dynamic stress changes at the rupture front but remains at very low
645 stress levels, experiencing a mild stress overshoot and no healing in contrast to the self-healing
646 pulse.

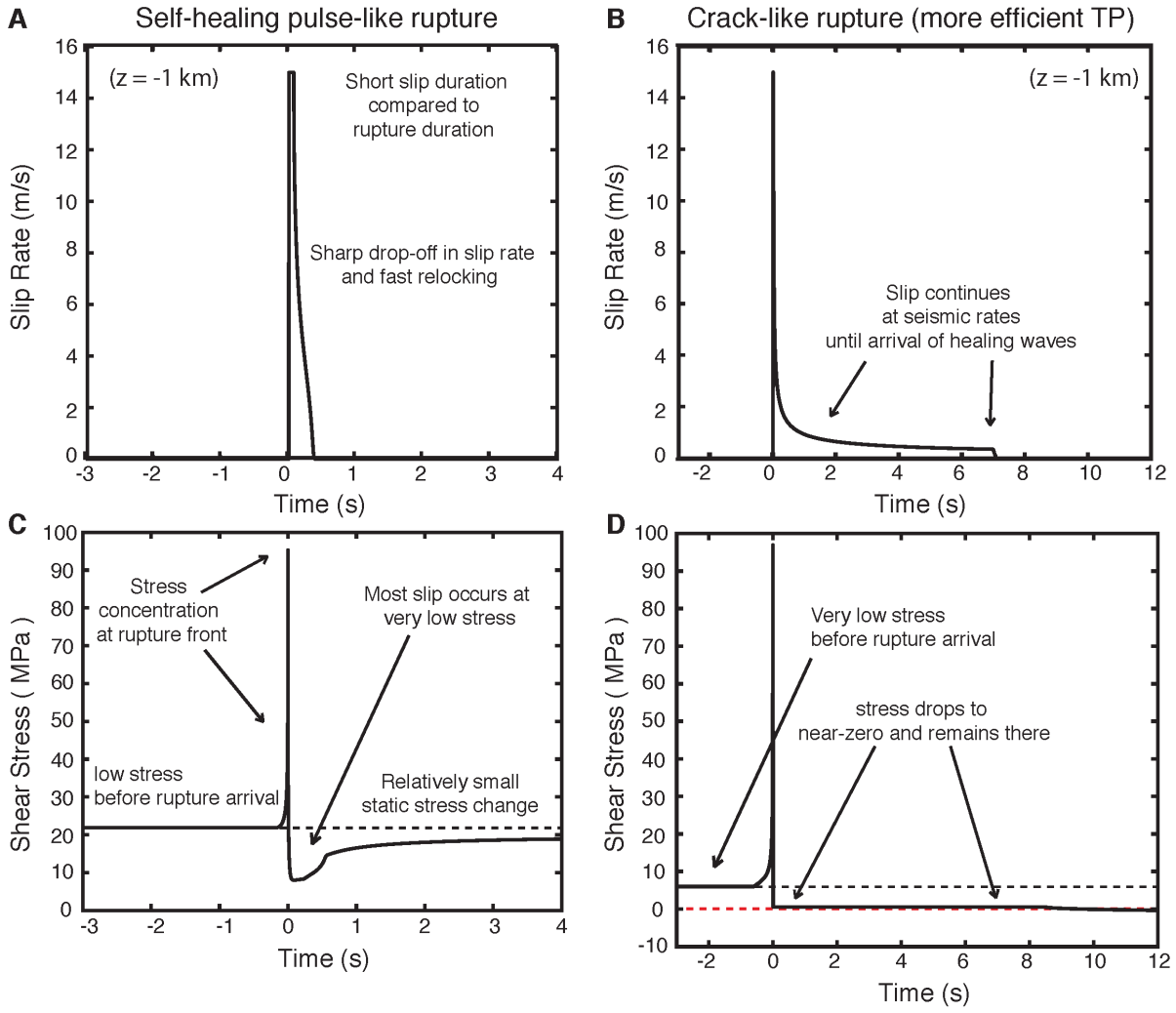

Fig. S9: Local behavior during a self-healing pulse and crack-like rupture. (A-B) Evolution of slip rate with time at an individual point in the center of a self-healing pulse-like rupture (A) and crack-like rupture (B) with more efficient enhanced weakening. Both ruptures experience a rapid acceleration of slip as the rupture front arrives, however, local sliding is very short in the self-healing pulse-like rupture before the point quickly relocks, whereas the point continues to slip with seismic slip rates (1 m/s) until the arrival of healing waves from the boundary in the crack-like rupture. (C-D) Evolution of shear stress with time for the same points as in (A-B). Both points have initially low prestress before the arrival of the stress concentration at the rupture front. The self-healing pulse dramatically weakens and then heals such that the static stress change is much smaller than the dynamic stress change. In contrast, the shear stress at the point in the crack-like rupture drops dramatically and stays low, such that the local static and dynamic stress drops are comparable.

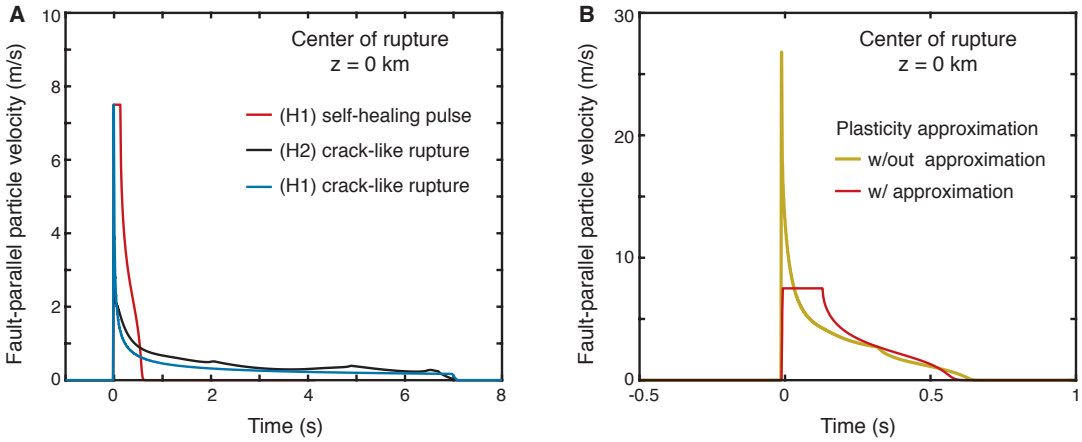

Fig. S10: Particle motion for self-healing pulse and crack-like ruptures. (A) Particle velocity vs. time in the center of the rupture region (z = 0) for a representative self-healing pulse on a quasi-statically strong, dynamically weak fault (H1,red, Fig. 2C), crack-like rupture on a persistently weak fault (H2, black, Fig. 2D), and crack-like rupture on a quasi-statically strong, dynamically weak fault (H1, blue, Fig. S8D). (B) The approximation of off-fault plasticity (V_{lim} = 15 m/s) reduces the sharp peak in particle velocity associated with the passing of the rupture front, which corresponds to high frequency motion above 1 Hz (Fig. S11C-D).

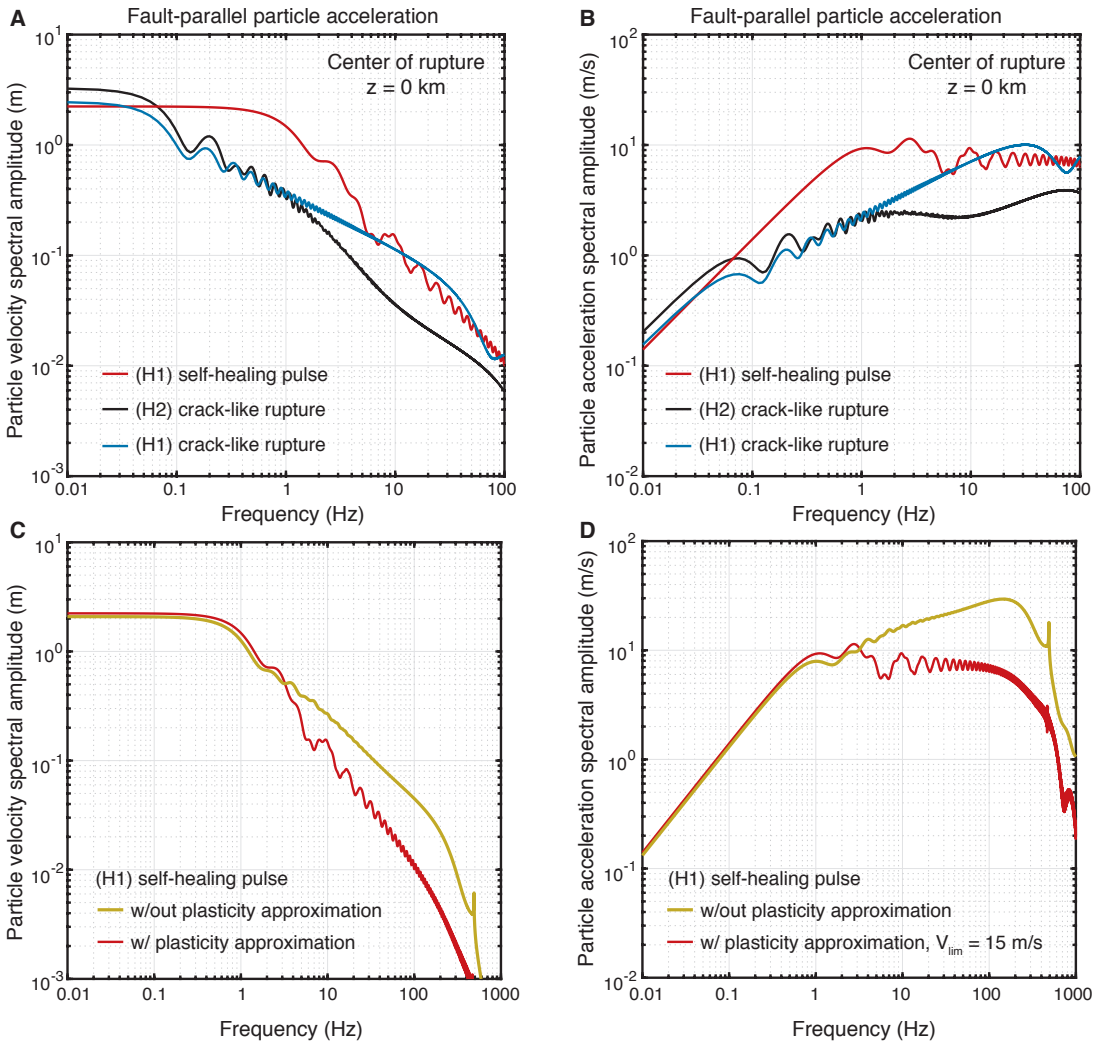

Fig. S11: Particle motion spectra for self-healing pulse and crack-like ruptures. (A-B) Particle velocity and acceleration spectral amplitudes in the center of the rupture region (z = 0) for a representative self-healing pulse on a quasi-statically strong, dynamically weak fault (H1, red, Fig. 2C), crack-like rupture on a persistently weak fault (H2, black, Fig. 2D), and crack-like rupture on a quasi-statically strong, dynamically weak fault (H1, blue, Fig. S8D). Both ruptures on quasi-statically strong, dynamically weak faults experience larger and more rapid dynamic stress changes resulting in more pronounced high-frequency ground motion above 1 Hz. (C-D) High-frequency motions can be considerably damped by the inclusion of approximations for off-fault plasticity (V_{lim} = 15 m/s), however this may be concentrated towards higher frequencies than typically considered for many seismological and strong ground motion studies.

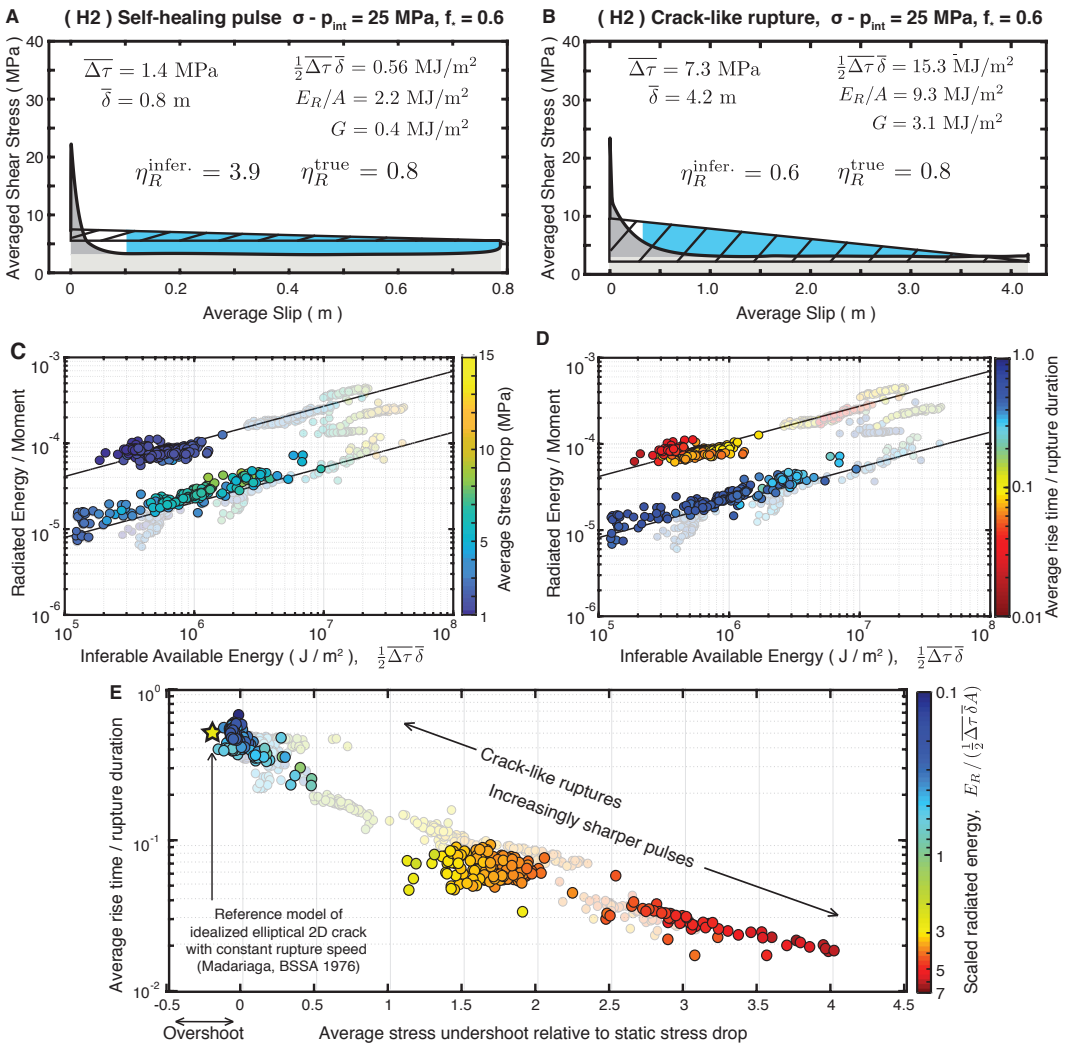

679

680 **Fig. S12: Self-healing pulses and crack-like ruptures in models with comparable quasi-static**
681 **strength.** (A-B) The average evolution of shear stress vs. slip for a representative self-healing
682 pulse and crack-like rupture with the same low quasi-static strength conditions (the effective nor-
683 mal stress of 25 MPa, models TP6a and TP 7b. The self-healing pulse results in a smaller static
684 stress drop and average slip than the crack-like rupture with similar quasi-static strength and com-
685 parable dynamic resistance. However, the self-healing pulse has a considerable undershoot com-
686 pared to its static stress drop. (C-D) Despite simulated self-healing pulses having lower average
687 static stress drops than crack-like ruptures with the same quasi-static strength and comparable dy-
688 namic resistance, the radiated energy to moment ratios for the pulse-like ruptures are much larger
689 than those for the crack-like ruptures. E) Progressively sharper pulses experience greater average
690 stress undershoot, resulting in more radiated energy for the same static stress drop and moment. In
691 panels (C-E), the grayed-out backgrounds show results from all models as in Fig. 2.

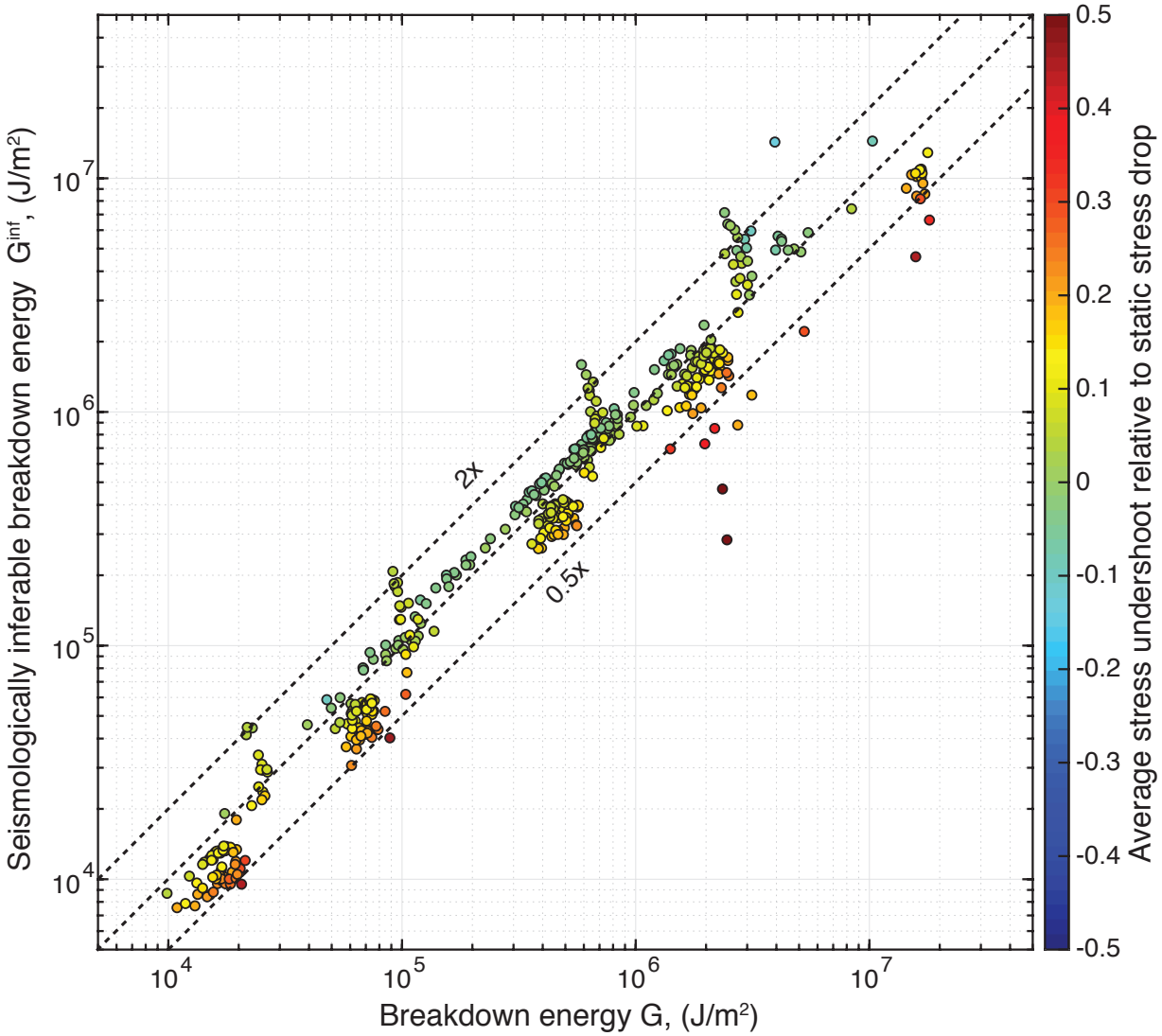

Fig. S13: Seismologically-inferable versus true breakdown energies for crack-like ruptures. Comparison of seismologically-inferable and true average breakdown energies for simulated crack-like ruptures with average stress overshoot/undershoot within $0.5\overline{\Delta\tau}$. Inferable breakdown energies are comparable to the true values, within a factor of two.

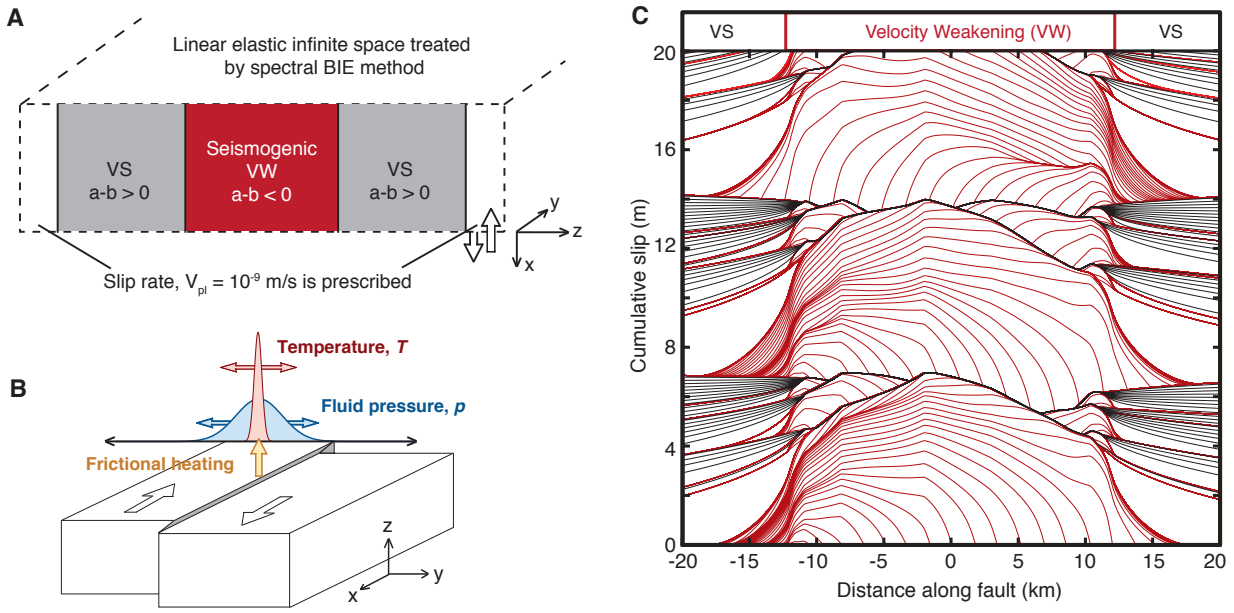

Fig. S14. Model set up for simulations of earthquake sequences and slow slip with and without enhanced dynamic weakening. (A) The fault is composed of a velocity-weakening (VW) seismogenic region surrounded by two velocity-strengthening (VS) sections. A fixed plate rate is prescribed outside of these regions. (B) We incorporate enhanced dynamic weakening due to the thermal pressurization of pore fluids by calculating the evolution of temperature and pore fluid pressure due to shear heating and off-fault diffusion throughout our simulations. (C) A short section of the accumulated slip history for simulated sequences of crack-like earthquake ruptures and aseismic slip from the same simulation as rupture of Figure 2. Seismic events are illustrated in with red lines plotted every 0.5 seconds while interseismic slip is plotted in black every 10 years.

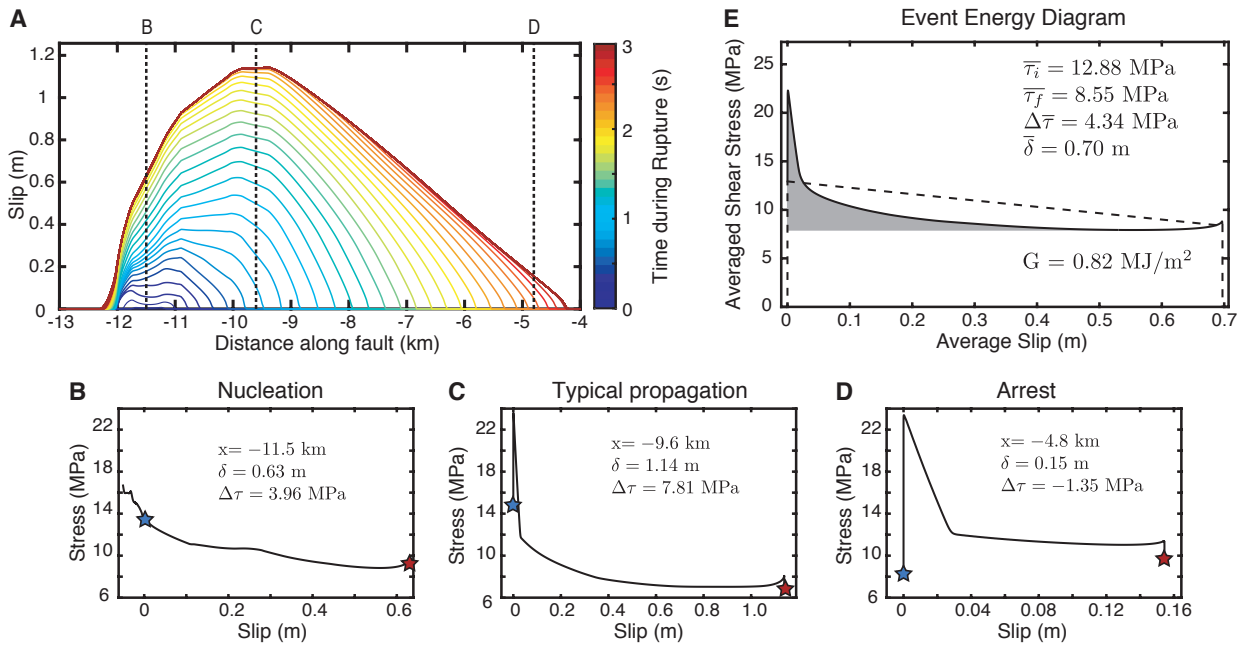

Fig S15: Averaging local on-fault behavior for entire rupture, for comparison with seismological observations. (A) Evolution of accumulated slip during a representative crack-like rupture with thermal pressurization. (B-D) The local evolution of shear stress with slip at three representative points showing: (B) the milder stress evolution during initial nucleation including preslip, (C) stress concentration followed by continuous weakening during typical rupture propagation, and (D) negative static stress drop near the arrest of the rupture. (E) Average shear stress vs. slip behavior which resembles the shape of the typical propagation location. The local behavior in all ruptures is variable, however we use the averaging methodology of (Noda and Lapusta, 2012) to construct the average shear stress vs. slip behavior and illustrate averaged source parameters.

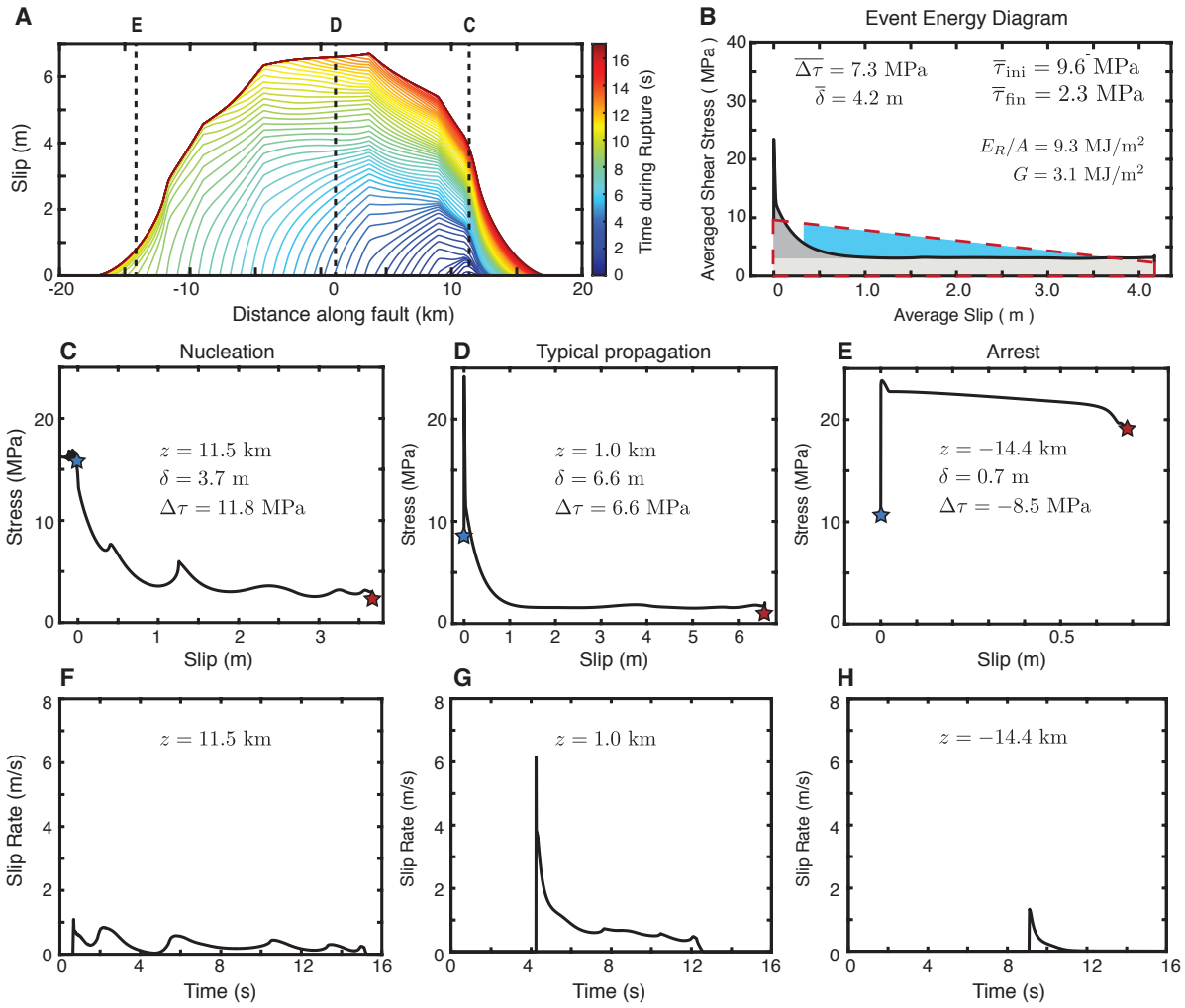

719

720 **Fig S16: Relationship between local and average stress versus slip behavior for a crack-like**
721 **rupture.** (A) Evolution of accumulated slip during a representative crack-like rupture with thermal
722 pressurization TP6a. Slip is contoured every 0.25 s. (B) Average shear stress vs. slip behavior. The
723 local behavior in all ruptures is variable, however we use the averaging methodology of Noda and
724 Lapusta (2012) to construct the average shear stress vs. slip behavior and illustrate averaged source
725 parameters. (C-E) The local evolution of shear stress with slip at three different points throughout
726 the rupture. (F-H) The local evolution of slip rate with time at the same points.

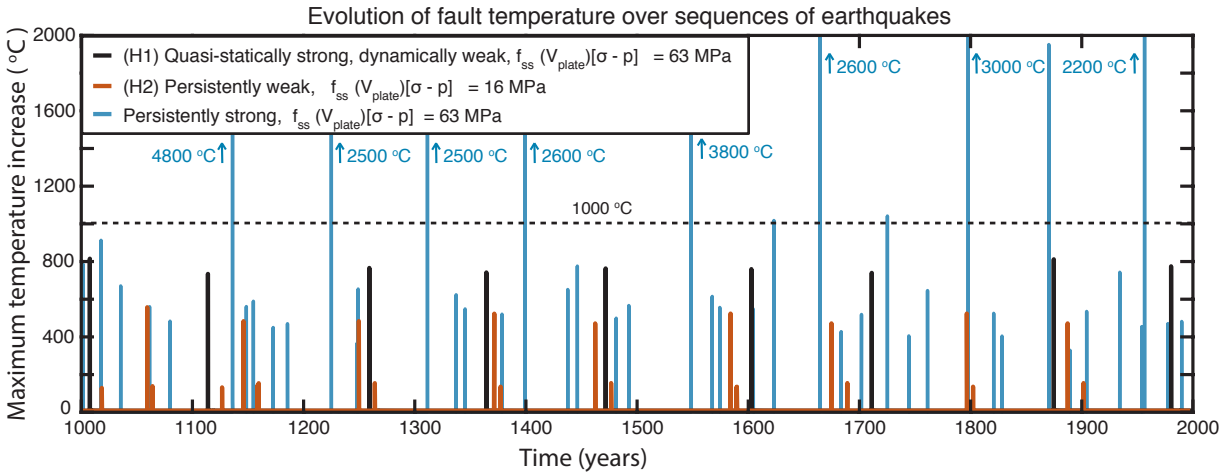

Fig. S17. Monitoring changes in fault temperature throughout sequences of earthquakes. The history of maximum temperature increase along the fault during the three simulations shown in Figure 3B-C in the main text. The three fault models are representative cases for (H1) a quasi-statically strong, dynamically weak fault (black lines), (H2) a persistently weak fault (red lines), and a persistently strong fault (blue lines). The models consistent with low-heat, low-stress hypothesis (H1) and (H2) maintain maximum temperature changes below 1000^o C, whereas the temperature changes for the persistently strong fault routinely increases over 2000^o C during large ruptures, given the shear zone width of 10 mm. Note that we can reduce the maximum fault temperatures in the persistently strong fault model by increasing the width of the shearing zone.

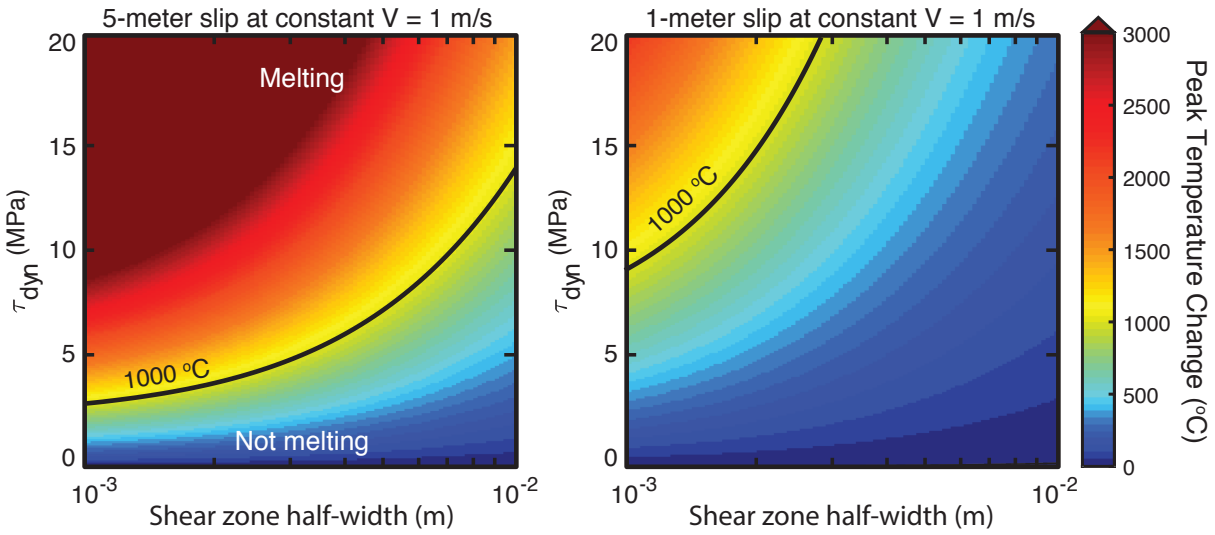

Fig. S18. Expected temperature rise due to shear heating. Peak temperature rise at varying dynamic levels of shear resistance and degrees of shear localization after 5 meters (right) and 1 meter (left) of slip at a fixed slip velocity of 1 m/s. For shear localized within layers of 1 mm half-width, resistance levels must be lower than 10 MPa even for 1 meter of slip to avoid temperature rises above 1000 ^{0}C.

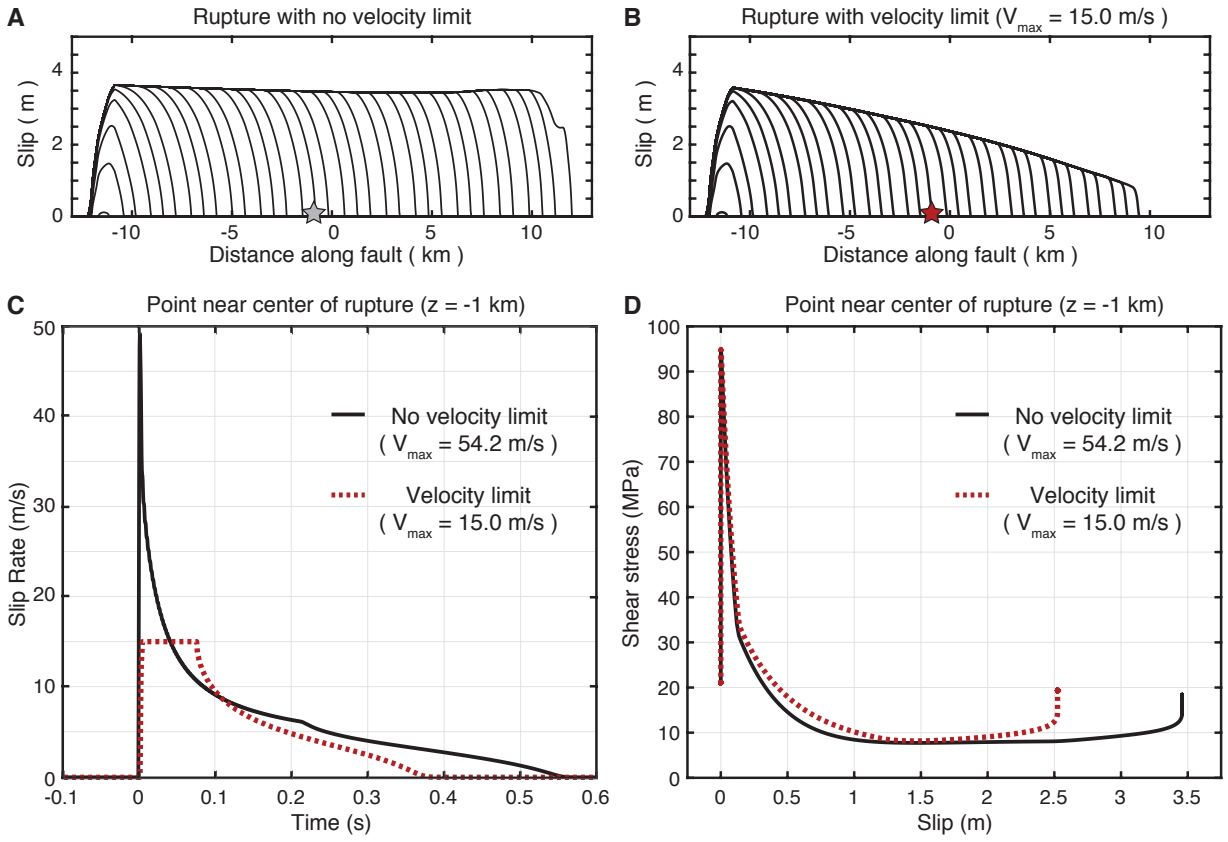

743

744 **Fig. S19: Using local velocity limit as an approximation for off-fault plasticity.** (A-B) Ac-
745 cumulation of slip during two dynamic ruptures with the same prestress in simulations without
746 (A) and with (B) an imposed velocity limit utilized to mimic effects of off-fault plasticity. (C-D)
747 Local slip rate versus time (C) and shear stress versus slip (D) at a point near the center of the
748 simulated ruptures (denoted by star in A and B). The initial weakening behavior is preserved for a
749 velocity limit of 15 m/s, however, the restricted dynamics lowers the weakening rate, increases the
750 breakdown energy G, limits the amount of slip during the rupture, resulting in a milder pulse.

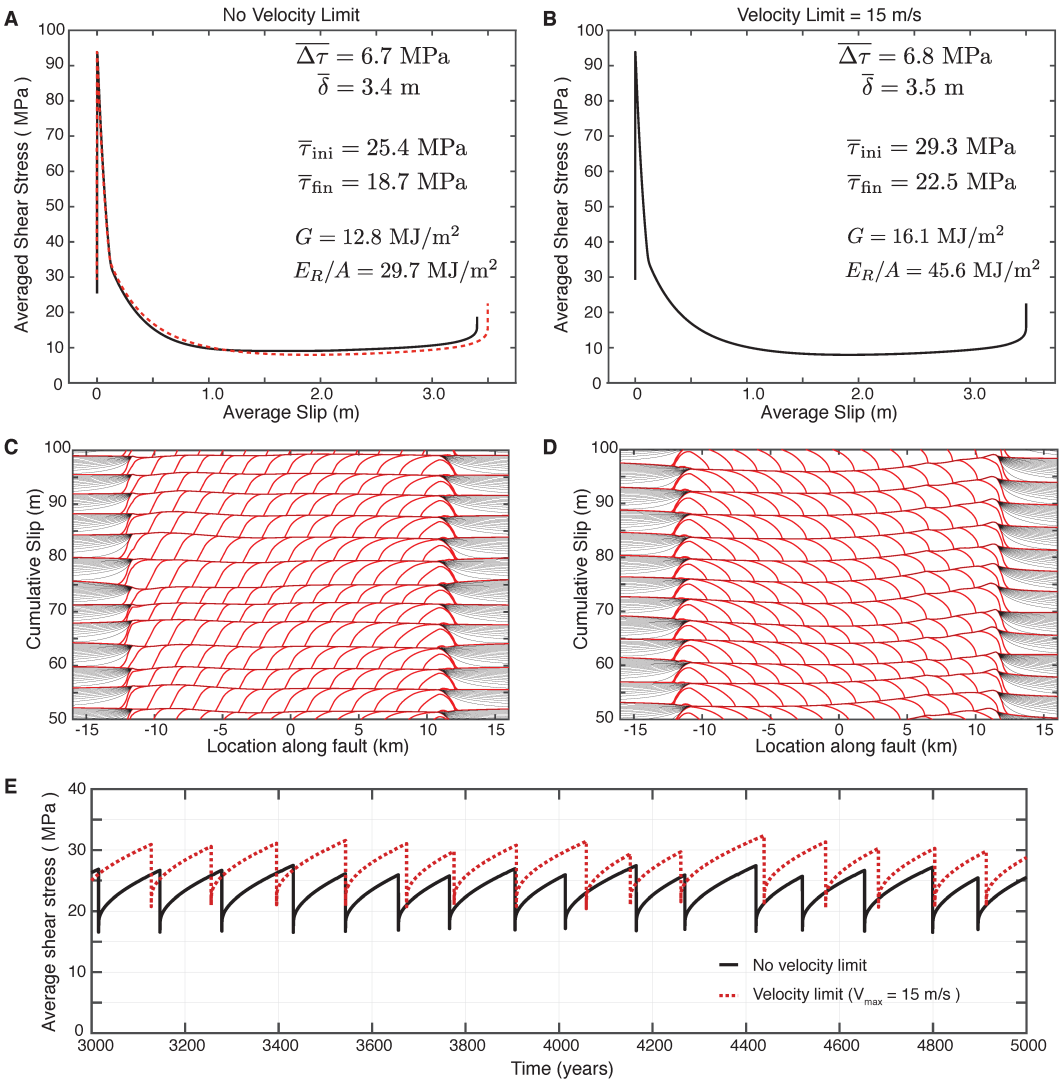

751

752 **Fig. S20: Long-term behavior of simulations with velocity limit.** (A-B) Average shear stress vs.
753 slip diagrams for events with similar stress drop and slip after long-term simulations of sequences
754 of seismic and aseismic slip without (A) and with (B) a velocity limit to mimic the effects of
755 off-fault plasticity. The average curve for the rupture with the velocity limit in (B) is overlain
756 on (A) as a red-dashed contour for comparison. Initial weakening is generally consistent but is
757 constrained by the velocity limit, resulting in more continuous weakening and mildly larger G.
758 The higher initial stress also results in greater overall undershoot and higher E_R/A. (C-D) The
759 general accumulation of slip within each event is similar for the long-term behavior of simulations
760 without (C) and with (D) the velocity limit. (E) The average shear stress is higher in simulations
761 with the velocity limit, which overcompensates for the additional effects due to limited velocity

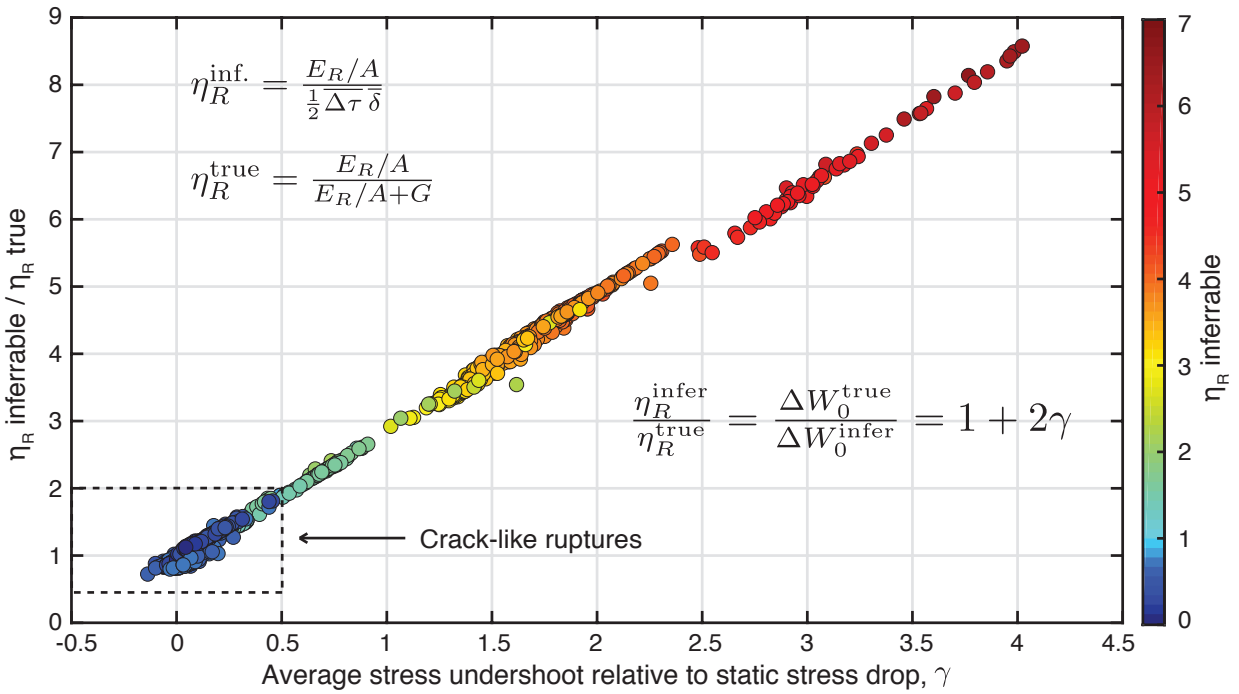

762

763 **Fig. S21: Relationship between radiation efficiency, available energy and stress undershoot.**
764 Comparison of seismologically-inferable and true radiation efficiencies as a function of stress un-
765 dershoot. As the average undershoot exceeds 0.5 of the static stress drop, the inferable radiation
766 efficiency exceeds the true efficiency by more than a factor of 2.

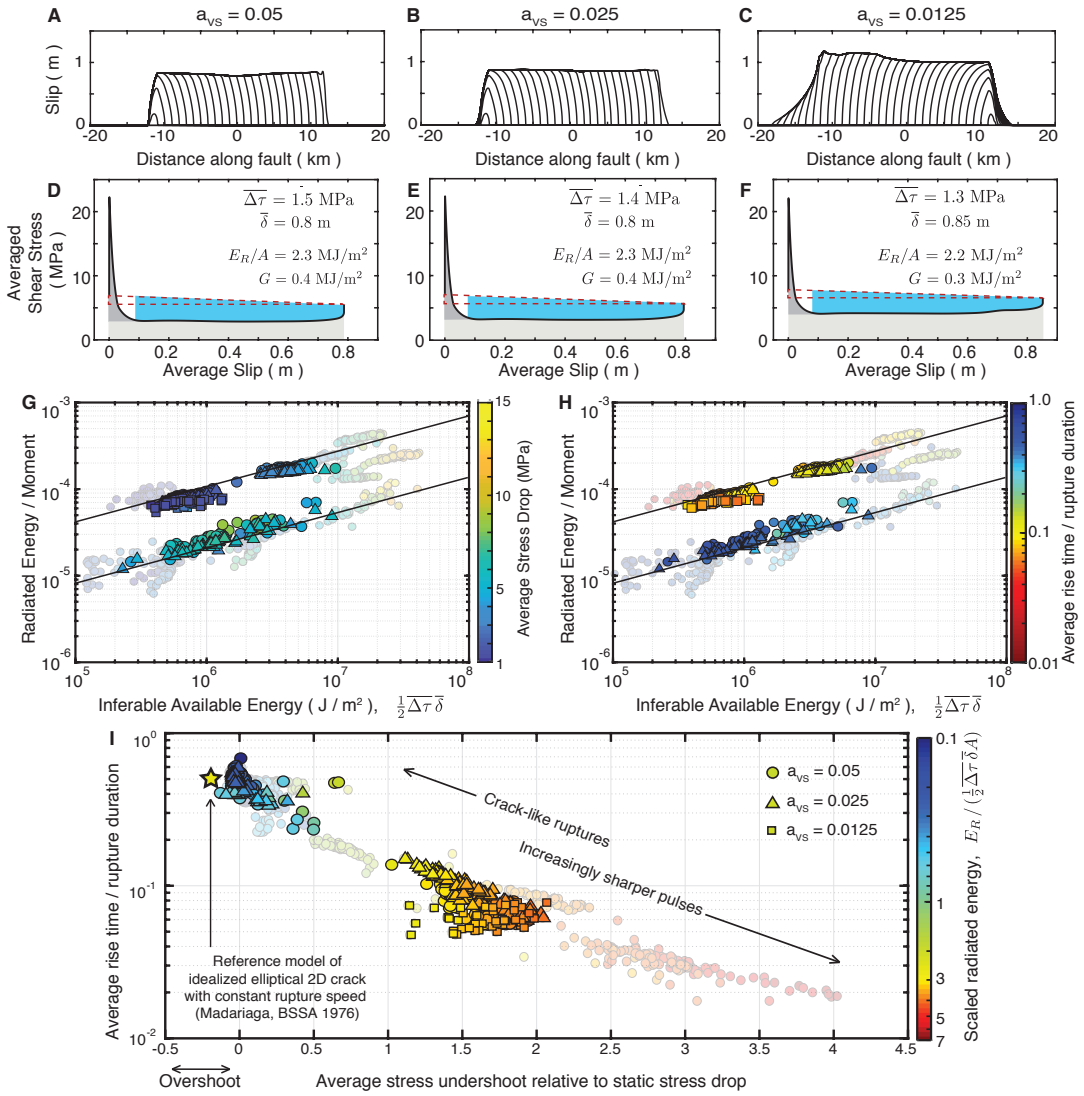

Fig. S22. Effect of velocity-strengthening regions on average source properties. (A-C) Representative self-healing pulses with comparable average slip in models TP7 with varying VS properties. (D-F) Corresponding average stress-slip diagrams that illustrate the energy partitioning for the ruptures in (A-C). Regions with strong VS properties ($a_{VS} = 0.05$) arrest rupture propagation over shorter distances than those with relatively weaker VS properties ($a_{VS} = 0.0125$), resulting in mild differences in average source properties such as the average slip and stress drop. (G-I) The scaling relationships between the average source properties are generally consistent among models with varying VS properties (TP 4,6 and 7), with ruptures exhibiting larger average undershoot radiating more energy for the same static stress drop and average slip. Models with relatively strong VS properties ($a_{VS} = 0.05$) are denoted by circles, while models with $a_{VS} = 0.025$ and $a_{VS} = 0.0125$ are denoted by triangles and squares, respectively. The grayed-out backgrounds show results from all models as in Fig. 2.

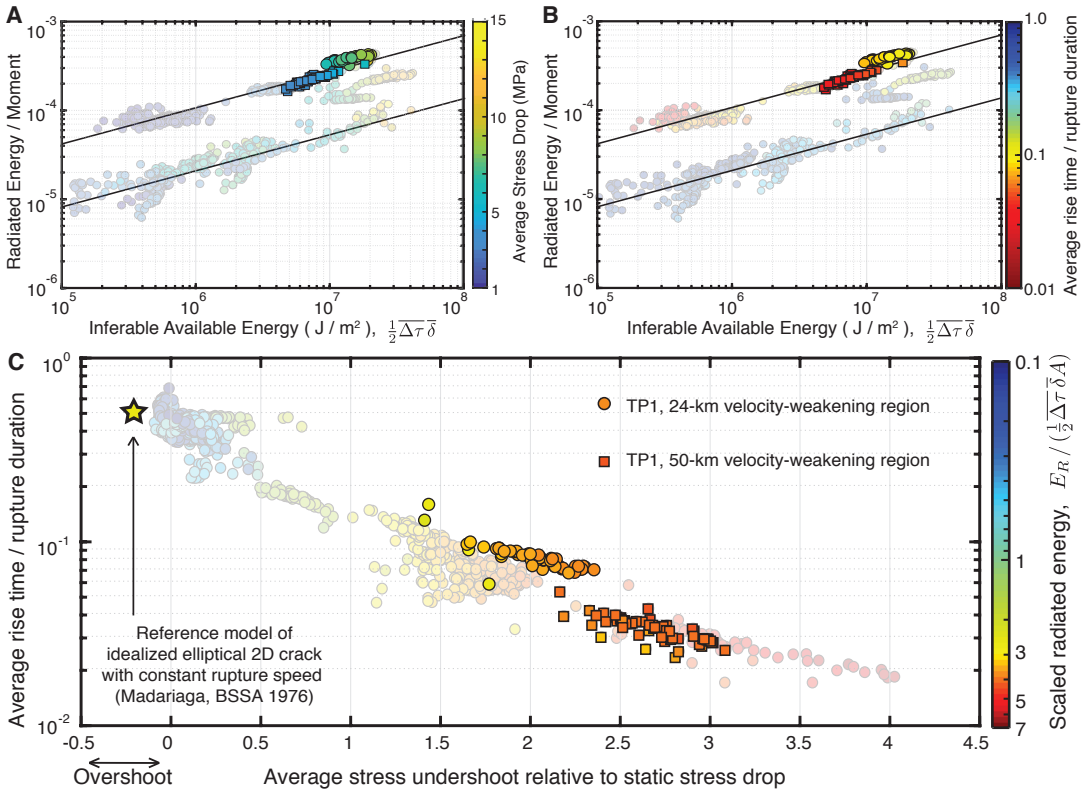

780

781 **Fig. S23: Consistency of radiated energy scaling for different fault lengths.** (A-B) Self-healing
782 pulses propagating over a 50-km VW region (squares) result in systematically lower static stress
783 drops than those propagating over a 24-km VW region and result in mildly sharper pulses with
784 shorter rise time to rupture duration. C) While the specific slip and stress distributions for different
785 rupture sizes vary, they exhibit a consistent trend in higher radiated energy with increasing stress
786 undershoot for the same average slip and stress.

Parameter	Symbol	Value
Loading slip rate	V_{plate}	10^{-9} m/s
Shear wave speed	c_s	3299 m/s
Shear modulus	μ	36 GPa
Thermal diffusivity	α_{th}	10^{-6} m^2/s
Specific heat	ρc	2.7 MPa/K
Rate-and-state parameters		
Reference slip velocity	V_*	10^{-6} m/s
Reference friction coefficient	f_*	0.6
Rate-and-state direct effect (VW)	a	0.010
Rate-and-state evolution effect (VW)	b	0.015
Rate-and-state direct effect (VS)	a	0.050
Rate-and-state evolution effect (VS)	b	0.003
Length scales		
Fault length	λ	96 km
Frictional domain	λ_{fr}	72 km
Velocity-weakening region	λ_{VW}	24 km
Cell size	Δz	3.3 m
Quasi-static cohesive zone	Λ_0	84 m
Nucleation size (Rice & Ruina, 1983)	h^*_{RR}	226 m
Nucleation size (Rubin & Ampuero, 2005)	h^*_{RA}	550 m

Table S1: Parameters for all simulations unless specified otherwise.

Parameter	Symbol	RS 1	RS 2	RS 3	RS 4
Interseismic effective normal stress	$\bar{\sigma} = (\sigma - p_{\text{int}})$	100 MPa	50 MPa	20 MPa	10 MPa
Reference friction coefficient	f_*	0.12	0.12	0.6	0.6
Characteristic slip	L	5 mm	2.5 mm	1 mm	0.5 mm
Shear zone half-width	w	10 mm	1 mm	10 mm	1mm
Quasi-static cohesive zone	Λ_0	106 m	106m	106 m	106 m
Nucleation size (Rice & Ruina, 1983)	h^*_{RR}	282 m	282 m	282 m	282 m
Nucleation size (Rubin & Ampuero, 2005)	h^*_{RA}	688 m	688 m	688 m	688 m

Table S2: Parameters for models with only standard rate-and-state friction, without enhanced dynamic weakening.

Parameter	Symbol	TP 1	TP 2	TP3
Interseismic effective normal stress	$\bar{\sigma} = (\sigma - p_{\text{int}})$	100 MPa	100 MPa	100 MPa
Rate-and-state direct effect (VS)	a	0.05	0.05	0.05
Characteristic slip	L	4 mm	4 mm	4 mm
Shear zone half-width	w	10 mm	10 mm	10 mm
Hydraulic diffusivity	α_{hy}	10^{-3} m^2/s	10^{-4} m^2/s	10^{-5} m^2/s
Coupling coefficient	Λ	0.34 MPa/K	0.34 MPa/K	0.34 MPa/K
		TP 4ab	TP 5	
Interseismic effective normal stress	$\bar{\sigma} = (\sigma - p_{\text{int}})$	50 MPa	50 MPa	
Rate-and-state direct effect (VS)	a	0.025, 0.05	0.05	
Characteristic slip	L	2 mm	2 mm	
Shear zone half-width	w	1 mm	1 mm	
Hydraulic diffusivity	α_{hy}	10^{-4}m^2/s	10^{-5} m^2/s	
Coupling coefficient	Λ	0.34 MPa/K	0.34 MPa/K	
		TP 6ab	TP 7abc	TP8
Interseismic effective normal stress	$\bar{\sigma} = (\sigma - p_{\text{int}})$	25 MPa	25 MPa	25 MPa
Rate-and-state direct effect (VS)	a	0.025, 0.05	0.0125, 0.025, 0.05	0.05
Characteristic slip	L	1 mm	1 mm	1 mm
Shear zone half-width	w	10 mm	1 mm	10 mm
Hydraulic diffusivity	α_{hy}	10^{-4}m^2/s	10^{-4}m^2/s	10^{-4} m^2/s
Coupling coefficient	Λ	0.34 MPa/K	0.34 MPa/K	0.1 MPa/K

Table S3: Parameters for models with thermal pressurization of pore fluids.

Parameter	Symbol	FW1
Interseismic effective normal stress	$\bar{\sigma} = (\sigma - p_{\text{int}})$	25 MPa
Characteristic slip	L	1 mm
Shear zone half-width	w	1 mm
Characteristic weakening velocity	V_w	0.14 m/s
Residual dynamic friction	f_w	0.12

Table S4: Parameters for models with flash weakening.

Parameter	Symbol	M2
Fault length	λ	192 km
Frictional domain	λ_{fr}	168 km
Velocity-weakening region	λ_{VW}	50 km
Cell size	Δz	3.3 m

Table S5: Length scales for longer fault model with thermal pressurization parameters TP1.

Earthquake	Refs	E_R^t (J)	E_R^r (J)	M_0 (N-m)	L x W (km)	$\overline{\delta}$ (m)	$\overline{\Delta\tau}_M$ (MPa)
San Fernando 1971	[21,72,73]	–	1.5e+15	7.0e+18	12 x 14	1.2	8.1
Coyote Lake 1979	[21,72,73]	–	4.6e+13	3.5e+17	6 x 6	0.5	4.1
Imperial Valley 1979	[26,74]	–	5.9e+14	6.7e+18	35 x 15	0.4	1.7
Morgan Hill 1986	[21,72,73]	–	1.4e+14	2.1e+18	20 x 8	0.4	2.9
Loma Prieta 1989	[26,75]	5.4e+14	2.7e+15	3.1e+19	40 x 17	1.5	4.8
Landers 1992	[26,76]	3.0e+15	1.2e+16	7.7e+19	65 x 15	2.6	7.6
Northridge 1994	[26,77]	3.1e+14	1.2e+15	1.3e+19	15 x 20	1.4	6.3
Kobe 1995	[26,78]	8.5e+14	1.5e15	2.4e+19	60 x 20	0.7	1.7
Hector Mine 1999	[26,79]	2.6e+15	3.2e+15	6.3e+19	41 x 13	3.9	15.5
Tottori 2000	[80,81]	1.8e+15	1.3e+15	1.2e+19	30 x 20	0.7	2.3
Denali 2002	[82,83]	3.6e+16	–	7.6e+20	292 x 18	4.8	10.4
Fukuoka 2005	[84,85]	–	6.5e+14	1.2e+19	26 x 18	0.9	3.3
Kumamoto 2016	[48,86]	–	2.1e+15	5.1e+19	40 x 15	2.8	9.5
Izmit 1999	[87,88]	6.0e+15	–	2.1e20	70 x 15	6.7	18.6

Table S6: Seismologically inferred source parameters for large crustal earthquakes compiled and derived from the indicated references. Radiated energy estimate is denoted as regional E_R^r or teleseismic E_R^t, where available. The rupture length L and width W are approximated from slip distributions of finite fault inversions in the given references. Average slip is estimated from these parameters as $\overline{\delta} = M_0/(\mu A)$, with rigidity $\mu = 3 \times 10^{10}$ N-m^{-2}, and the moment-based stress drop is estimated as a rectangular source region as $\overline{\Delta\tau}_M = CM_0/A^{3/2}$, where C takes values of 2.53, 3.02, and 5.21 for aspect ratios of 1, 4 and 16, respectively[68].

Video S1: Evolution of shear stress during a self-healing pulse-like rupture on a quasi-statically strong but dynamically weak fault.
Evolution of shear stress (black line) along the fault during a self-healing pulse-like rupture on a quasi-statically strong but dynamically weak fault (H1). The video illustrates the changes in shear stress with respect to the initial (gray) and final (blue) shear stresses, as well as the quasi-static strength (red). The initial stress on the majority of the fault is far below the quasi-static strength, except for the region in which the rupture nucleates, which is small compared to the total rupture area. As the rupture front crosses the seismogenic (VW) region, each point experiences a large dynamic stress increase towards $\sim$100 MPa and then drops to low levels below 10 MPa. Only a small portion of the fault slips at a given time as the shear resistance heals behind the rupture front and the fault relocks, resulting in higher final stress levels than the level of shear resistance at which most of the slip occurred.

Video S2: Evolution of shear stress during a crack-like rupture on a persistently weak fault.
Evolution of shear stress (black line) along the fault during a mild crack-like rupture on a persistently weak fault (H2). The initial shear stress over the entire rupture region is within 1-2 times the static stress drop (7.3 MPa) away from the quasi-static strength. Slip continues within the regions behind the rupture front until the rupture front is arrested in the VS region on the other side of the seismogenic (VW) region, and healing waves redistribute stress and arrest slip. All conventions follow Video S1.

Video S3: Scaled evolution of shear stress during a crack-like rupture rupture on a persistently weak fault.
Evolution of shear stress (black line) along the fault for the same mild crack-like rupture as shown in Video S2, however with the shear stress axis rescaled to emphasize the dynamic stress changes during the rupture. Slip continues within the regions behind the rupture front until the rupture front is arrested in the VS region on the other side of the seismogenic (VW) region, and healing waves redistribute stress and arrest slip, resulting in a dynamic overshoot throughout most of the ruptured region. All conventions follow Videos S1 and S2.

1. Brune, J. N., Henyey, T. L. & Roy, R. F. Heat flow, stress, and rate of slip along the San Andreas Fault, California. *Journal of Geophysical Research* **74**, 3821–3827 (1969).

2. Henyey, T. L. & Wasserburg, G. J. Heat flow near major strike-slip faults in California. *Journal of Geophysical Research (1896-1977)* **76**, 7924–7946 (1971).

3. Sibson, R. H. Generation of pseudotachylyte by ancient seismic faulting. *Geophysical Journal of the Royal Astronomical Society* **43**, 775–794 (1975).

4. Lachenbruch, A. H. & Sass, J. H. Heat flow and energetics of the San Andreas Fault Zone. *Journal of Geophysical Research: Solid Earth* **85**, 6185–6222 (1980).

5. Townend, J. & Zoback, M. D. Regional tectonic stress near the San Andreas fault in central and Southern California. *Geophysical Research Letters* **31** (2004).

6. Rice, J. R. Heating and weakening of faults during earthquake slip. *Journal of Geophysical Research* **111**, B05311 (2006).

7. Suppe, J. Absolute fault and crustal strength from wedge tapers. *Geology* **35**, 1127–1130 (2007).

8. Tanikawa, W. & Shimamoto, T. Frictional and transport properties of the Chelungpu fault from shallow borehole data and their correlation with seismic behavior during the 1999 Chi-Chi earthquake. *Journal of Geophysical Research: Solid Earth* **114** (2009).

9. Nankali, H. R. Slip rate of the Kazerun Fault and Main Recent Fault (Zagros, Iran) from 3D mechanical modeling. *Journal of Asian Earth Sciences* **41**, 89–98 (2011).

10. Fulton, P. M. *et al.* Low coseismic friction on the Tohoku-Oki fault determined from temperature measurements. *Science* **342**, 1214–1217 (2013).

11. Gao, X. & Wang, K. Strength of stick-slip and creeping subduction megathrusts from heat flow observations. *Science* **345**, 1038–1041 (2014).

12. Chester, F. M. & Chester, J. S. Ultracataclasite structure and friction processes of the Punchbowl fault, San Andreas system, California. *Tectonophysics* **295**, 199 – 221 (1998).

13. Wibberley, C. A. & Shimamoto, T. Earthquake slip weakening and asperities explained by thermal pressurization. *Nature* **436**, 689–692 (2005).

14. Tullis, T. Friction of rock at earthquake slip rates. *Treatise on Geophysics* **4**, 131–152 (2007).

15. Di Toro, G. *et al.* Fault lubrication during earthquakes. *Nature* **471**, 494 (2011).

16. Brown, K., Kopf, A., Underwood, M. & Weinberger, J. Compositional and fluid pressure controls on the state of stress on the Nankai subduction thrust: A weak plate boundary. *Earth and Planetary Science Letters* **214**, 589 – 603 (2003).

17. Faulkner, D. R., Mitchell, T. M., Healy, D. & Heap, M. J. Slip on 'weak' faults by the rotation of regional stress in the fracture damage zone. *Nature* **444**, 922–925 (2006).

18. Bangs, N. *et al.* Broad, weak regions of the Nankai Megathrust and implications for shallow coseismic slip. *Earth and Planetary Science Letters* **284**, 44 – 49 (2009).

19. Collettini, C., Niemeijer, A., Viti, C. & Marone, C. Fault zone fabric and fault weakness. *Nature* **462**, 907–910 (2009).

20. Lockner, D. A., Morrow, C., Moore, D. & Hickman, S. Low strength of deep san andreas fault gouge from SAFOD core. *Nature* **472**, 82–85 (2011).

21. Heaton, T. H. Evidence for and implications of self-healing pulses of slip in earthquake rupture. *Physics of the Earth and Planetary Interiors* **64**, 1–20 (1990).

22. Noda, H., Dunham, E. M. & Rice, J. R. Earthquake ruptures with thermal weakening and the operation of major faults at low overall stress levels. *Journal of Geophysical Research: Solid Earth* **114** (2009).

23. Allmann, B. P. & Shearer, P. M. Global variations of stress drop for moderate to large earthquakes. *Journal of Geophysical Research: Solid Earth* **114** (2009).

24. Ye, L., Lay, T., Kanamori, H. & Rivera, L. Rupture characteristics of major and great (Mw $>$ 7.0) megathrust earthquakes from 1990 to 2015: 2. depth dependence. *Journal of Geophysical Research: Solid Earth* **121**, 845–863 (2016).

25. Ide, S. & Beroza, G. C. Does apparent stress vary with earthquake size? *Geophysical Research Letters* **28**, 3349–3352 (2001).

26. Abercrombie, R. E. & Rice, J. R. Can observations of earthquake scaling constrain slip weakening? *Geophysical Journal International* **162**, 406–424 (2005).

27. Viesca, R. C. & Garagash, D. I. Ubiquitous weakening of faults due to thermal pressurization. *Nature Geoscience* **8**, 875–879 (2015).

28. Perry, S. M., Lambert, V. & Lapusta, N. Nearly magnitude-invariant stress drops in simulated crack-like earthquake sequences on rate-and-state faults with thermal pressurization of pore fluids. *Journal of Geophysical Research: Solid Earth* **125**, e2019JB018597 (2020).

29. Beeler, N. M., Wong, T. F. & Hickman, S. H. On the expected relationships among apparent stress, static stress drop, effective shear fracture energy, and efficiency. *Bulletin of the Seismological Society of America* **93**, 1381–1389 (2003).

30. Kanamori, H. & Rivera, L. Energy partitioning during an earthquake. *Earthquakes: Radiated energy and the physics of faulting* 3–13 (2006).

31. Madariaga, R. Dynamics of an expanding circular fault. *Bulletin of the Seismological Society of America* **66**, 639–666 (1976).

32. Noda, H. & Lapusta, N. Three-dimensional earthquake sequence simulations with evolving temperature and pore pressure due to shear heating: Effect of heterogeneous hydraulic diffusivity. *Journal of Geophysical Research* **115**, B123414 (2010).

33. Dieterich, J. Applications of rate- and state-dependent friction to models of fault slip and earthquake occurrence. In Schubert, G. (ed.) *Treatise on Geophysics*, 107 – 129 (Elsevier, Amsterdam, 2007).

34. Andrews, D. J. Rupture Models with Dynamically Determined Breakdown Displacement. *Bulletin of the Seismological Society of America* **94**, 769–775 (2004).

35. Noda, H. & Lapusta, N. On averaging interface response during dynamic rupture and energy partitioning diagrams for earthquakes. *Journal of Applied Mechanics* **79** (2012).

36. Choy, G. L. & Boatwright, J. L. Global patterns of radiated seismic energy and apparent stress. *Journal of Geophysical Research: Solid Earth* **100**, 18205–18228 (1995).

37. Perez-Campos, X. & Beroza, G. C. An apparent mechanism dependence of radiated seismic energy. *Journal of Geophysical Research: Solid Earth* **106**, 11127–11136 (2001).

38. Ma, S. & Archuleta, R. J. Radiated seismic energy based on dynamic rupture models of faulting. *Journal of Geophysical Research: Solid Earth* **111** (2006).

39. Perrin, G., Rice, J. R. & Zheng, G. Self-healing slip pulse on a frictional surface. *Journal of the Mechanics and Physics of Solids* **43**, 1461 – 1495 (1995).

40. Day, S. M. Three-dimensional finite difference simulation of fault dynamics: Rectangular faults with fixed rupture velocity. *Bulletin of the Seismological Society of America* **72**, 705–727 (1982).

41. Beroza, G. C. & Mikumo, T. Short slip duration in dynamic rupture in the presence of heterogeneous fault properties. *Journal of Geophysical Research: Solid Earth* **101**, 22449–22460 (1996).

42. Andrews, D. J. & Ben-Zion, Y. Wrinkle-like slip pulse on a fault between different materials. *Journal of Geophysical Research: Solid Earth* **102**, 553–571 (1997).

43. Kanamori, H. & Brodsky, E. E. The physics of earthquakes. *Reports on Progress in Physics* **67**, 1429–1496 (2004).

44. Cocco, M., Bizzarri, A. & Tinti, E. Physical interpretation of the breakdown process using a rate-and state-dependent friction law. *Tectonophysics* **378**, 241–262 (2004).

45. Savage, J. C. & Wood, M. D. The relation between apparent stress and stress drop. *Bulletin of the Seismological Society of America* **61**, 1381–1388 (1971).

46. Rice, J. R., Sammis, C. G. & Parsons, R. Off-Fault Secondary Failure Induced by a Dynamic Slip Pulse. *Bulletin of the Seismological Society of America* **95**, 109–134 (2005).

47. Jiang, J. & Lapusta, N. Deeper penetration of large earthquakes on seismically quiescent faults. *Science* **352**, 1293–1297 (2016).

48. Kanamori, H., Ross, Z. E. & Rivera, L. Estimation of radiated energy using the KiK-net downhole records - Old method for modern data. *Geophysical Journal International* (2020).

49. Lapusta, N., Rice, J. R., Ben-Zion, Y. & Zheng, G. Elastodynamic analysis for slow tectonic loading with spontaneous rupture episodes on faults with rate- and state- dependent friction. *Journal of Geophysical Research* **105**, 765–789 (2000).

50. Dieterich, J. H. Modeling of rock friction 1. experimental results and constitutive equations. *Journal of Geophysical Research* **84**, 2161–2168 (1979).

51. Ruina, A. Slip instability and state variable friction laws. *Journal of Geophysical Research* **88**, 10359–10370 (1983).

52. Noda, H. Frictional constitutive law at intermediate slip rates accounting for flash heating and thermally activated slip process. *Journal of Geophysical Research: Solid Earth* **113** (2008).

53. Marone, C. Laboratory-derived friction laws and their application to seismic faulting. *Annual Review of Earth and Planetary Sciences* **26**, 643–696 (1998).

54. Bhattacharya, P., Rubin, A. M., Bayart, E., Savage, H. M. & Marone, C. Critical evaluation of state evolution laws in rate and state friction: Fitting large velocity steps in simulated fault gouge with time-, slip-, and stress-dependent constitutive laws. *Journal of Geophysical Research: Solid Earth* **120**, 6365–6385 (2015).

55. Sibson, R. H. Interactions between temperature and pore-fluid pressure during earthquake faulting and a mechanism for partial or total stress relief. *Nature* **243**, 66–68 (1973).

56. Segall, P., Rubin, A. M., Bradley, A. M. & Rice, J. R. Dilatant strengthening as a mechanism for slow slip events. *Journal of Geophysical Research: Solid Earth* **115** (2010).

57. Rempel, A. W. & Rice, J. R. Thermal pressurization and onset of melting in fault zones. *Journal of Geophysical Research: Solid Earth* **111** (2006).

58. Dunham, E. M., Belanger, D., Cong, L. & Kozdon, J. E. Earthquake Ruptures with Strongly Rate-Weakening Friction and Off-Fault Plasticity, Part1: Planar Faults. *Bulletin of the Seismological Society of America* **101**, 2296–2307 (2011).

59. Han, R., Shimamoto, T., Ando, J.-i. & Ree, J.-H. Seismic slip record in carbonate-bearing fault zones: An insight from high-velocity friction experiments on siderite gouge. *Geology* **35**, 1131–1134 (2007).

60. Sulem, J. & Famin, V. Thermal decomposition of carbonates in fault zones: Slip-weakening and temperature-limiting effects. *Journal of Geophysical Research: Solid Earth* **114** (2009).

61. Goldsby, D. L. & Tullis, T. E. Low frictional strength of quartz rocks at subseismic slip rates. *Geophysical Research Letters* **29**, 25–1–25–4 (2002).

62. Di Toro, G., Goldsby, D. L. & Tullis, T. E. Friction falls towards zero in quartz rock as slip velocity approaches seismic rates. *Nature* **427**, 436–439 (2004).

63. Brodsky, E. E. & Kanamori, H. Elastohydrodynamic lubrication of faults. *Journal of Geophysical Research: Solid Earth* **106**, 16357–16374 (2001).

64. Rice, J. & Ruina, A. L. Stability of steady frictional slipping. *Journal of Applied Mechanics* **50**, 343–349 (1983).

65. Rubin, A. & Ampuero, J.-P. Earthquake nucleation on (aging) rate and state faults. *Journal of Geophysical Research: Solid Earth* **110** (2005).

66. Day, S. M., Dalguer, L. A., Lapusta, N. & Liu, Y. Comparison of finite difference and boundary integral solutions to three-dimensional spontaneous rupture. *Journal of Geophysical Research: Solid Earth* **110** (2005).

67. Noda, H. & Lapusta, N. Stable creeping fault segments can become destructive as a result of dynamic weakening. *Nature* **493**, 518 EP – (2013).

68. Noda, H., Lapusta, N. & Kanamori, H. Comparison of average stress drop measures for ruptures with heterogeneous stress change and implications for earthquake physics. *Geophysical Journal International* (2013).

69. Liu, P. & Archuleta, R. Inversions for kinematic source parameters of the 1994 Northridge earthquake using a three dimensional velocity structure. *Seism. Res. Lett* **71**, 220 (2000).

70. Tinti, E., Scognamiglio, L., Michelini, A. & Cocco, M. Slip heterogeneity and directivity of the ML 6.0, 2016, Amatrice earthquake estimated with rapid finite-fault inversion. *Geophysical Research Letters* **43** (2016).

71. Adams, M., Twardzik, C. & Ji, C. Exploring the uncertainty range of coseismic stress drop estimations of large earthquakes using finite fault inversions. *Geophysical Journal International* **208**, 86–100 (2016).

72. Bolt, B. A. Seismic energy release over a broad frequency band. *Pure and Applied Geophysics* **124**, 919–930 (1986).

73. Smith, K. D., Brune, J. N. & Priestley, K. F. The seismic spectrum, radiated energy, and the Savage and Wood inequality for complex earthquakes. *Tectonophysics* **188**, 303 – 320 (1991).

74. Archuleta, R. J. A faulting model for the 1979 Imperial Valley earthquake. *Journal of Geophysical Research: Solid Earth* **89**, 4559–4585 (1984).

75. Wald, D. J., Helmberger, D. V. & Heaton, T. H. Rupture model of the 1989 Loma Prieta earthquake from the inversion of strong-motion and broadband teleseismic data. *Bulletin of the Seismological Society of America* **81**, 1540–1572 (1991).

76. Wald, D. J. & Heaton, T. H. Spatial and temporal distribution of slip for the 1992 Landers, California, earthquake. *Bulletin of the Seismological Society of America* **84**, 668–691 (1994).

77. Wald, D. J., Heaton, T. H. & Hudnut, K. W. The slip history of the 1994 Northridge, California, earthquake determined from strong-motion, teleseismic, GPS, and leveling data. *Bulletin of the Seismological Society of America* **86**, S49–S70 (1996).

78. Wald, D. J. A Preliminary Dislocation Model for the 1995 Kobe (Hyogo-ken Nanbu), Japan, Earthquake Determined from Strong Motion and Teleseismic Waveforms. *Seismological Research Letters* **66**, 22–28 (1995).

79. Ji, C., Wald, D. J. & Helmberger, D. V. Source Description of the 1999 Hector Mine, California, Earthquake, Part II: Complexity of Slip History. *Bulletin of the Seismological Society of America* **92**, 1208–1226 (2002).

80. Tinti, E., Spudich, P. & Cocco, M. Earthquake fracture energy inferred from kinematic rupture models on extended faults. *Journal of Geophysical Research: Solid Earth* **110** (2005).

81. Choy, G. L. & Boatwright, J. Differential Energy Radiation from Two Earthquakes in Japan with Identical Mw: The Kyushu 1996 and Tottori 2000 Earthquakes. *Bulletin of the Seismological Society of America* **99**, 1815–1826 (2009).

82. Asano, K., Iwata, T. & Irikura, K. Estimation of Source Rupture Process and Strong Ground Motion Simulation of the 2002 Denali, Alaska, Earthquake. *Bulletin of the Seismological Society of America* **95**, 1701–1715 (2005).

83. Choy, G. L. & Boatwright, J. Radiated Energy and the Rupture Process of the Denali Fault Earthquake Sequence of 2002 from Broadband Teleseismic Body Waves. *Bulletin of the Seismological Society of America* **94**, S269–S277 (2004).

84. Asano, K. & Iwata, T. Source process and near-source ground motions of the 2005 West Off Fukuoka Prefecture earthquake. *Earth, Planets and Space* **58**, 93–98 (2006).

85. Yoo, S.-H., Rhie, J., Choi, H. & Mayeda, K. Evidence for non-self-similarity and transitional increment of scaled energy in the 2005 west off Fukuoka seismic sequence. *Journal of Geophysical Research: Solid Earth* **115** (2010).

86. Asano, K. & Iwata, T. Source rupture processes of the foreshock and mainshock in the 2016 Kumamoto earthquake sequence estimated from the kinematic waveform inversion of strong motion data. *Earth, Planets and Space* **68**, 147 (2016).

87. Yagi, Y. & Kikuchi, M. Source rupture process of the Kocaeli, Turkey, earthquake of August 17, 1999, obtained by joint inversion of near-field data and teleseismic data. *Geophysical Research Letters* **27**, 1969–1972 (2000).

88. Kanamori, H. & Ross, Z. E. Reviving mB. *Geophysical Journal International* **216**, 1798–1816 (2019).

89. Kostrov, B. Self-similar problems of propagation of shear cracks. *Journal of Applied Mathematics and Mechanics* **28**, 1077 – 1087 (1964).

90. Kostrov, B. Seismic moment and energy of earthquakes and seismic flow of rock. *Izv. Acad. Sci. USSR Phys. Solid Earth* **1**, 23–44 (1974).

91. Husseini, M. I. & Randall, M. J. Rupture velocity and radiation efficiency. *Bulletin of the Seismological Society of America* **66**, 1173–1187 (1976).

92. Dahlen, F. A. The balance of energy in earthquake faulting. *Geophysical Journal of the Royal Astronomical Society* **48**, 239–261 (1977).

93. Boatwright, J. & Choy, G. L. Teleseismic estimates of the energy radiated by shallow earthquakes. *Journal of Geophysical Research: Solid Earth* **91**, 2095–2112 (1986).

94. Kostrov, B. V. & Das, S. *Principles of earthquake source mechanics* (Cambridge, England ; New York : Cambridge University Press, 1988).

95. Venkataraman, A. & Kanamori, H. Observational constraints on the fracture energy of subduction zone earthquakes. *Journal of Geophysical Research: Solid Earth* **109** (2004).

96. Palmer, A. C. & Rice, J. The growth of slip surfaces in the progressive failure of over-consolidated clay. *Proceedings of the Royal Society of London A: Mathematical, Physical and Engineering Sciences* **332**, 527–548 (1973).

97. Kanamori, H. & Heaton, T. H. Microscopic and macroscopic physics of earthquakes. *Geocomplexity and the Physics of Earthquakes* 147–163 (2000).

98. Wyss, M. & Brune, J. N. Seismic moment, stress, and source dimensions for earthquakes in the california-nevada region. *Journal of Geophysical Research (1896-1977)* **73**, 4681–4694 (1968).

99. McGarr, A. On relating apparent stress to the stress causing earthquake fault slip. *Journal of Geophysical Research: Solid Earth* **104**, 3003–3011 (1999).

100. Wei, M. & McGuire, J. J. The Mw 6.5 offshore Northern California earthquake of 10 January 2010: Ordinary stress drop on a high-strength fault. *Geophysical Research Letters* **41**, 6367–6373 (2014).

101. Gabriel, A.-A., Ampuero, J.-P., Dalguer, L. A. & Mai, P. M. The transition of dynamic rupture styles in elastic media under velocity-weakening friction. *Journal of Geophysical Research: Solid Earth* **117** (2012).

102. Brantut, N., Garagash, D. I. & Noda, H. Stability of pulse-like earthquake ruptures. *Journal of Geophysical Research: Solid Earth* **124**, 8998–9020 (2019).

103. Zheng, G. & Rice, J. R. Conditions under which velocity-weakening friction allows a self-healing versus a crack-like mode of rupture. *Bulletin of the Seismological Society of America* **88**, 1466–1483 (1998).

104. Dunham, E. M., Belanger, D., Cong, L. & Kozdon, J. E. Earthquake Ruptures with Strongly Rate-Weakening Friction and Off-Fault Plasticity, Part 2: Nonplanar Faults. *The Bulletin of the Seismological Society of America* **101**, 2308–2322 (2011).